International Journal of Heat and Mass Transfer 214 (2023) 124324

Contents lists available at ScienceDirect

International Journal of Heat and Mass Transfer

journal homepage: www.elsevier.com/locate/hmt

Reynolds stresses and turbulent heat fluxes in fan-shaped and cylindrical film cooling holes

Muting Hao[1,*], Luca di Mare[1]

Oxford Thermofluids Institute, University of Oxford, Southwell Building, Osney Mead, Oxford, OX2 0ES, United Kingdom

ARTICLE INFO

Article history:
Received 3 November 2022
Revised 9 May 2023
Accepted 16 May 2023
Available online 19 June 2023

Keywords:
Film cooling
Heat transfer
Gas turbines
Large eddy simulation
Reynolds stresses
Turbulent heat fluxes
Shaped holes

ABSTRACT

Large eddy simulation (LES) is carried out to predict the thermal performance, unsteady flow patterns, and turbulence characteristics of the fan-shaped hole and the cylindrical hole cooling films. Velocity fields, Reynolds stresses, and turbulent heat flux distributions are the factors that ultimately determine the film cooling effectiveness by deciding the concentration of coolant and heat near the surface. Accurate prediction of these processes can provide a reliable data set for the design of film cooling systems. It can also help solve difficulties of improving RANS-based simulations in terms of their inaccuracies in matching measured flow rates for a given pressure drop across the film and the mixing process once the coolant is ejected from the film. Credible estimates and modest costs of the current LES originate from the multiblock hexahedra meshing, the turbulence inflow generator, and the numerical schemes implemented. Multiblock hexahedra meshes are adopted and generated by a quasi-automatic mesh generation algorithm utilizing template-based multi-block construction followed by elliptic smoothing. Computational resources are utilized in a way that mesh refinement exists only near cooling decorations of small size and wall boundaries, without the need for associated clustering in the far field which is commonly used in commercial packages. The high orthogonality and continuous smoothness throughout the computational domain are maintained to facilitate turbulence capturing. The synthetic inflow generator produces a random field matching a realistic set of two-point statistics based on eigen-reconstruction in a computationally inexpensive processing step. To prove that the current LES simulations of modest cost can reproduce with high accuracy, the discharge characteristics, velocity, and turbulence intensity profiles of cylindrical and fan-shaped cooling films are compared with published measured data on the same flow configurations. Results reveal that the set of modeling methodologies is valid for calculating film-cooling performance within an acceptable range of accuracy. The energy-carrying turbulence structures in and near the cooling holes are shown and their behaviors are linked to turbulent Reynolds stresses. Reynolds stresses and turbulent heat fluxes are compared for different blowing ratios and two types of cooling holes in the parametric study. Similarity patterns of velocity profiles, non-dimensional temperature profiles, Reynolds stress and turbulent heat flux profiles are discussed.

© 2023 The Author(s). Published by Elsevier Ltd.
This is an open access article under the CC BY-NC-ND license
(http://creativecommons.org/licenses/by-nc-nd/4.0/)

1. Introduction

Cooling technologies have become key to improving gas turbine engine performance in aircraft propulsion, power generation, and industrial applications alike. Thermodynamic considerations encourage designers to use higher and higher turbine inlet gas temperatures, to improve both efficiency and power output. In order for modern gas turbines to safely operate at turbine inlet temperatures above the metal melting point, several cooling methods have been devised. A successful design for any cooling system uses less cooling air while pursuing lower metal temperatures. This is because whilst essential, turbine cooling comes at a thermodynamic price. Inappropriate amounts of cooling air result in a heavy penalty to thermal efficiency.

Film cooling is a popular method and consists in forming a thin layer of coolant around the component. The coolant is fed through small orifices on the component surface. The design of film cooling systems requires accurate estimates of the film discharge characteristics and of the mixing process of the coolant downstream of

* Corresponding author.
E-mail address: muting.hao@eng.ox.ac.uk (M. Hao).
[1] Oxford Thermofluids Institute, University of Oxford.

https://doi.org/10.1016/j.ijheatmasstransfer.2023.124324
0017-9310/© 2023 The Author(s). Published by Elsevier Ltd. This is an open access article under the CC BY-NC-ND license
(http://creativecommons.org/licenses/by-nc-nd/4.0/)

the films. This information is needed to formulate accurate predictions of the film effectiveness. Traditionally, this information could be extracted from correlations. Correlation-based tools, however, lack the flexibility required by modern designs and as a result, CFD calculations are deployed more and more often in the design of film cooling systems.

Most film cooling flow predictions are based on the Reynolds-averaged Navier-VStokes (RANS). The RANS method is a popular method due to its efficiency and relatively low computational cost. RANS are currently the predominant choice for simulating cooling applications of industrial interest. Despite continuous improvements in turbulence models in the past 40 years, RANS simulations of film cooling generally suffer from issues such as over-prediction of the penetration distance into the mainstream (see Hoda and Acharya [1]) and the under-prediction of the coolant jet spreading rate. These inaccuracies originate from the poor performance of RANS model in flows with large density variations and strong streamline curvature. Both these features are present in the flow generated by film cooling devices.

To improve RANS modeling, a systematic set of Reynolds stress data are needed. Also, it is these Reynolds stresses that determine how the coolant flows downstream. To solve these problems, Large eddy simulation (LES) can be relied on. Therefore, LES becomes important, not only for its more accurate predictions of heat load and end-wall flow structures but also because the information such as Reynolds stresses that can be provided by LES are crucial in improving turbulence models of RANS simulations.

LES studies on film cooling have become increasingly popular recently. [2] studied the flow structures along a cylindrical cooling hole, which is selected from Sinha et al. [3] experiment, by a large-eddy simulation. A deep understanding of the mixing process was provided. However, a simplification of the turbulent boundary layer of inflow to a time-averaged profile prevents them from capturing realistic mixing processes suitably. Oliver et al. [15] found the Mach number of coolant flow may be several times higher than the mainstream Mach number, and the resulting compressibility will influence the cooling performance. They gave an explanation of the decomposed mechanisms in the cooling holes in LES results of laterally-expanded holes under two Mach number conditions. [4] studied the effect of blowing ratio and incline angle through LES. They observed that the counter-rotating vortex is more downstream in an inclined angle of 30 cases compared to a normal jet case. Renze et al. [5] studied the effect of density ratio on the attachment/recirculation by LES of the jet in crossflow. Gräf and Kleiser [6] carried out an LES study of double-row compound film cooling. Kong et al. [7] captured the details of flow structures in a film-cooled leading edge model. Chen et al. [8] simulated the evolution of hairpin vortices and instantaneous flow structures using LES. Wang et al. [9] combined deep learning with CFD methods to obtain film-cooling effectiveness. These studies focus on capturing the details of instantaneous flow structures by improving part of the numerical tool. However, in these studies, well-resolved profiles of velocity, Reynolds stresses and turbulent heat fluxes and the regularity pattern for them are barely explored. The requirement for the complete set of well-resolved profiles of these quantities for the design of the film cooling system provides the need for a reliable LES numerical tool that can provide these data of reliable quality.

Moreover, a parametric study of blowing ratios and cooling film hole geometries on the Reynolds stresses is significant. It can provide guidance for designers as it covers a wide range of mixing regimes. Recent RANS-based results [10] show that in most cases RANS predictions contain the correct asymptotic decay of quantities such as effectiveness, but the wrong level. If a parametric study could provide some indications on how the quantities such as Reynolds stress perform under different blowing ratios, modifications on the RANS model might be proposed to give equivalent accuracy of predictions as LES in film cooling.

In this study, LES is carried out to predict the thermal performance, unsteady flow patterns, and turbulence characteristics of the fan-shaped hole and the cylindrical hole cooling films. Simulations on various operating conditions, including an array of Mach numbers, blowing ratios, and orientation angles, are examined by being compared with classical experimental data. Reynolds stresses and turbulent heat fluxes are compared for different blowing ratios and two types of cooling holes in the parametric study. Similarity patterns of velocity profiles, non-dimensional temperature profiles, and Reynolds stresses profiles are discussed.

The structure of this study is arranged as below. Section 2 will introduce the computational details including the configuration, the meshing, the LES platform, and the setting up for simulations. Section 3 will provide validations in terms of meshing independence, the discharge coefficient, the mean profiles, the Reynolds stress, the film cooling effectiveness, and flowfield patterns. Section 4 will present the results and discussion of the flow field and a parametric study of Reynolds stresses and turbulent heat fluxes in film coolings with fan-shaped and cylindrical holes at different blowing ratios. Section 5 will summarize the conclusions.

2. Computational details

2.1. Flow configuration

The computations are based and validated on experimental data obtained in experiments described by Wittig et al (see Wittig et al. [11]). The flow conditions and geometries are selected to match those from the experiment by Thole et al (see Thole et al. [12]) and (see Gritsch [13]). Both fan-shaped and cylindrical film cooling holes are studied. Their geometries are shown in Fig. 1.

All the studied holes are inclined at 30°, with a hole length-to-diameter ratio of $L/D = 6$. An array of operating conditions with various blowing ratios, mainstream Mach numbers, and orientation angles are simulated. Table 1 shows the considered operating conditions for the current LES study. The availability of experimental data provided in the published references is also listed in Table 1. The data not available from experiments, especially Favre-averaged velocities and Reynolds stresses, can be provided in the current study. This is performed as the current study is attempting to extend the numerical approaches to complement the previously obtained experimental data. Although there are a few LES studies on a similar type of film cooling recently, for example, [14–18], a systematic set of Reynolds stress or turbulent heat flux data with well-resolved profiles is still few. Studies like [19] are early pioneers that provide Reynolds stress and turbulent heat flux data in film cooling flows from simple holes. A complete set of Reynolds

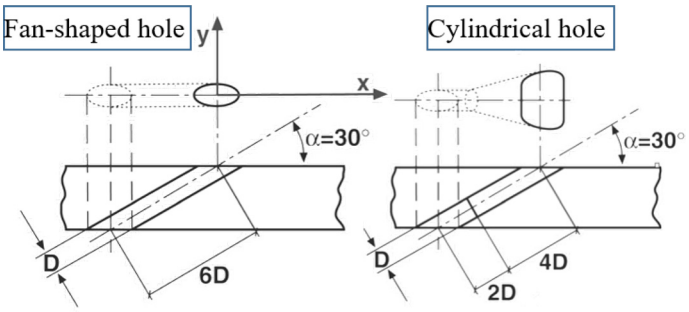

Fig. 1. The geometry of film cooling holes: left (a) fan-shaped hole, right (b) cylindrical hole after [12].

Table 1
List of available experimental data in published references.

	Case									Availability			
Geometry	T_{tc}	T_{tc}/T_m	Re_{Dm}	δ_{99}/D	Tu_m	Ma_m	Ma_c	β	M	D_c	η	Mean vel	Reynolds stresses
Fan-shaped	300*K*	1	$\leqslant 5.2 \cdot 10^4$	0.8	$\leq 1.5\%$	0.25	0.3	0	1.0	-	-	A	-
Cylindrical	300*K*	1	$\leqslant 5.2 \cdot 10^4$	0.8	$\leq 1.5\%$	0.25	0.3	0	1.0	-	-	A,D	A
Fan-shaped	290*K*	0.54	$\leqslant 1.3 \cdot 10^5$	0.5	$\leq 2\%$	0.6	0	0	0.5	B, E, F	C	-	-
Fan-shaped	290*K*	0.54	$\leqslant 1.3 \cdot 10^5$	0.5	$\leq 2\%$	0.6	0	0	0.5	B, E, F	C, G	-	-
Fan-shaped	290*K*	0.54	$\leqslant 1.3 \cdot 10^5$	0.5	$\leq 2\%$	0.6	0	0	0.5	B, E, F	C	-	-
Cylindrical	290*K*	0.54	$\leqslant 1.3 \cdot 10^5$	0.5	$\leq 2\%$	0.6	0	0	0.5	B, E, F	C	-	-
Cylindrical	290*K*	0.54	$\leqslant 1.3 \cdot 10^5$	0.5	$\leq 2\%$	0.6	0	0	1.0	B, E, F	C, G	-	-
Cylindrical	290*K*	0.54	$\leqslant 1.3 \cdot 10^5$	0.5	$\leq 2\%$	0.6	0	0	1.5	B, E, F	C	-	-
Fan-shaped	290*K*	0.54	$\leqslant 1.3 \cdot 10^5$	0.5	$\leq 2\%$	0.3	0	0	0.5	B, E, F	H	-	-
Fan-shaped	290*K*	0.54	$\leqslant 1.3 \cdot 10^5$	0.5	$\leq 2\%$	0.3	0	0	1.0	B, E, F	-	-	-
Fan-shaped	290*K*	0.54	$\leqslant 1.3 \cdot 10^5$	0.5	$\leq 2\%$	0.3	0	0	1.5	B, E, F	H	-	-
Cylindrical	290*K*	0.54	$\leqslant 1.3 \cdot 10^5$	0.5	$\leq 2\%$	0.3	0	0	0.5	B, E, F	H	-	-
Cylindrical	290*K*	0.54	$\leqslant 1.3 \cdot 10^5$	0.5	$\leq 2\%$	0.3	0	0	1.0	B, E, F	H	-	-
Cylindrical	290*K*	0.54	$\leqslant 1.3 \cdot 10^5$	0.5	$\leq 2\%$	0.3	0	0	1.5	B, E, F	H	-	-
Fan-shaped	290*K*	0.54	$\leqslant 1.3 \cdot 10^5$	0.5	$\leq 2\%$	0.6	0	90	0.5	E, F	-	-	-
Fan-shaped	290*K*	0.54	$\leqslant 1.3 \cdot 10^5$	0.5	$\leq 2\%$	0.6	0	90	1.0	E, F	-	-	-
Fan-shaped	290*K*	0.54	$\leqslant 1.3 \cdot 10^5$	0.5	$\leq 2\%$	0.6	0	90	1.5	E, F	-	-	-
Cylindrical	290*K*	0.54	$\leqslant 1.3 \cdot 10^5$	0.5	$\leq 2\%$	0.6	0	90	0.5	E, F	-	-	-
Cylindrical	290*K*	0.54	$\leqslant 1.3 \cdot 10^5$	0.5	$\leq 2\%$	0.6	0	90	1.0	E, F	-	-	-
Cylindrical	290*K*	0.54	$\leqslant 1.3 \cdot 10^5$	0.5	$\leq 2\%$	0.6	0	90	1.5	E, F	-	-	-

*A is Thole et al. [12]
*B is Gritsch et al. [20]
*C is Gritsch et al. [13]
*D is Thole et al. [21]
*E is Gritsch et al. [22]
*F is Gritsch et al. [23]
*G is SAUMWEBER et al. [24]
*H is Saumweber and Schulz [25]

Table 2
List of simulations.

	Case					Time	
Geometry	Ma_m	Ma_c	β	M	Mesh Size	Transient	Total
Fan-shaped	0.25	0.3	0	1.0	10534612	7f	191,100 chr
Cylindrical	0.25	0.3	0	1.0	10534612	7f	218,660 chr
Fan-shaped	0.6	0	0	0.5	10534612	12f	115,821 chr
Fan-shaped	0.6	0	0	1.0	10,534,612	13f	132,440 chr
Fan-shaped	0.6	0	0	1.5	10,534,612	12f	88,070 chr
Cylindrical	0.6	0	0	0.5	9,674,752	11f	156,594 chr
Cylindrical	0.6	0	0	1.0	9,674,752	10f	146,950 chr
Cylindrical	0.6	0	0	1.5	9,674,752	10f	142,750 chr
Fan-shaped	0.3	0	0	0.5	1,316,864	7f	8000 chr
Fan-shaped	0.3	0	0	1.0	1,316,864	7f	8000 chr
Fan-shaped	0.3	0	0	1.5	1,316,864	7f	8000 chr
Cylindrical	0.3	0	0	0.5	1,209,344	7f	9200 chr
Cylindrical	0.3	0	0	1.0	1,209,344	7f	9200 chr
Cylindrical	0.3	0	0	1.5	1209344	7f	9200 chr
Fan-shaped	0.6	0	90	0.5	1,105,920	10f	20,050 chr
Fan-shaped	0.6	0	90	1.0	1,105,920	10f	20,050 chr
Fan-shaped	0.6	0	90	1.5	1,105,920	10f	20,050 chr
Cylindrical	0.6	0	90	0.5	777,216	12f	9200 chr
Cylindrical	0.6	0	90	1.0	777,216	12f	9200 chr
Cylindrical	0.6	0	90	1.5	777,216	12f	9200 chr

*$1f = 1$ flow through time, $1chr = 1$ core hour

stress and turbulent heat flux data based on more types of cooling holes have not been explored enough.

Table 2 outlines the mesh size and the time consumed for the list of simulations used in Results and Discussions.

2.2. Grid arrangement

Body-fitted, multiblock hexahedral grids are generated by the mesh generator 'H4X' described in Hao et al. [26]. The mesh generator is a quasi-automatic mesh generation algorithm. The algorithm uses templates to construct multiblock grids around complex geometries. The grid is composed of suitably arranged blocks containing identical numbers of cells and joined by conformal interfaces. Because cooling films can be idealized as small-size holes extruded from the main flow passages, they are well suited to templated grid generation using a trunk and branch approach. The grids are smoothed elliptically. The smoothing method is then implemented on the resulting multiblock grids. It uses a modification of Thompson's Poisson system. Elliptic smoothing is performed on the boundaries as well as inside the volume. The position of grid points on the boundary surfaces is not fixed but is determined as a result of the smoothing process. Boundary orthogonality is enforced on all surfaces. Control functions are used to set the wall spacing in the direction orthogonal to the boundary sur-

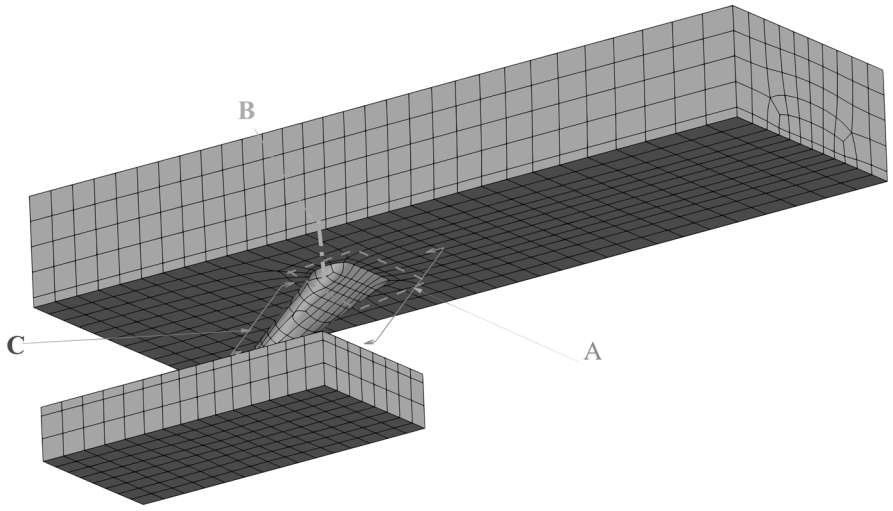

(a) Visualisation from the outside.

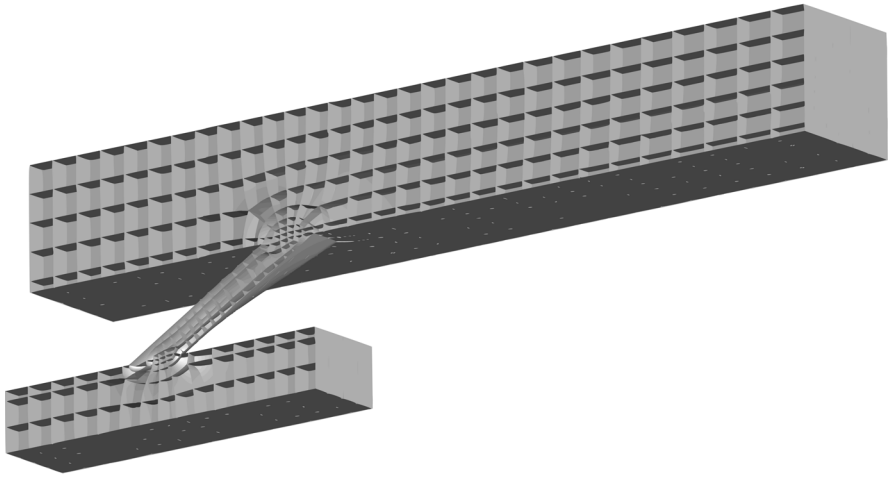

(b) Visualisation from the midsection.

Fig. 2. The layout of the fan-shaped cooling hole mesh.

faces. A Newton-like update for the control functions of the Poisson systems is relied on for the grid size control. Grid orthogonality and smoothness are guaranteed throughout the computational domains. The block layout can be optimized in such a way that the mesh is refined only near the cooling decorations and the wall boundaries, without the need for clustering extended into the far field which is common when using commercial meshing software.

The meshing procedure 1) starts by generating two trunk layouts for the hot stream channel and the coolant channel. 2) Suitable types of film are added as templated layouts to each block. 3) Once a layout is generated, hexahedral grids are immediately generated by splitting all blocks into the same number of cells. 4) The smoothing step maps each separated block onto the cooling hole geometry. 5) Two half-films that have been added separately onto the hot-stream and coolant channels are then joined together, with the patches of individual domains merged into the final configuration. 5) The mesh is optimized by operations such as local refinement, splitting, and collapse. 6) A round of smoothing is performed on the final layout to produce the mesh.

Fig. 2 shows the generated layout of the fan-shaped cooling film case with a parallel orientation between the mainstream channel and the coolant channel. The layout presents the block boundaries with every n^{th} point of the mesh. For example, for the most refined mesh used in this study, n is 24 in both types of film cases. As shown in Fig. 2, the layout in the transitional region is unstructured but smoothly transitioned. Fig. 3 shows the meshing used for collecting statistics. Meshing grids in different views corresponding to the sections in Fig. 2a are zoomed in. Fig. 3a which shows the smoothly allocated grids around the film. Fig. 3b, 3c, and 3d show that the grids in the transitional region of the cooling film are seamless, and smoothly distributed in each of the three directions. The mesh is orthogonal to the wall and orthogonal to the junction between the film and the mainstream. The layouts are generated in a way that there are 44 blocks on the connecting intersection across the fan-shaped film hole and 38 blocks on the connecting intersection across the cylindrical film hole. The value of $y+$ is below 1.6, as shown in Fig. 4. $\Delta x^+ \approx 29$. $\Delta z^+ \approx 20$.

A study of grid quality has been examined in Fig. 5 on five grid sizes when the node relocation displacement has arrived at the same residual level after the smoothing operation. Fig. 5 shows that 90% of grid cells have unit scales of Jacobian for all the considered meshes of both the cylindrical and the fan-shaped holes.

A well-smoothed mesh of $8 \times 8 \times 8$ cells per block can be generally employed for simulations if only a coarse boundary layer resolution is required. So the mesh of 8x8x8 cells per block is

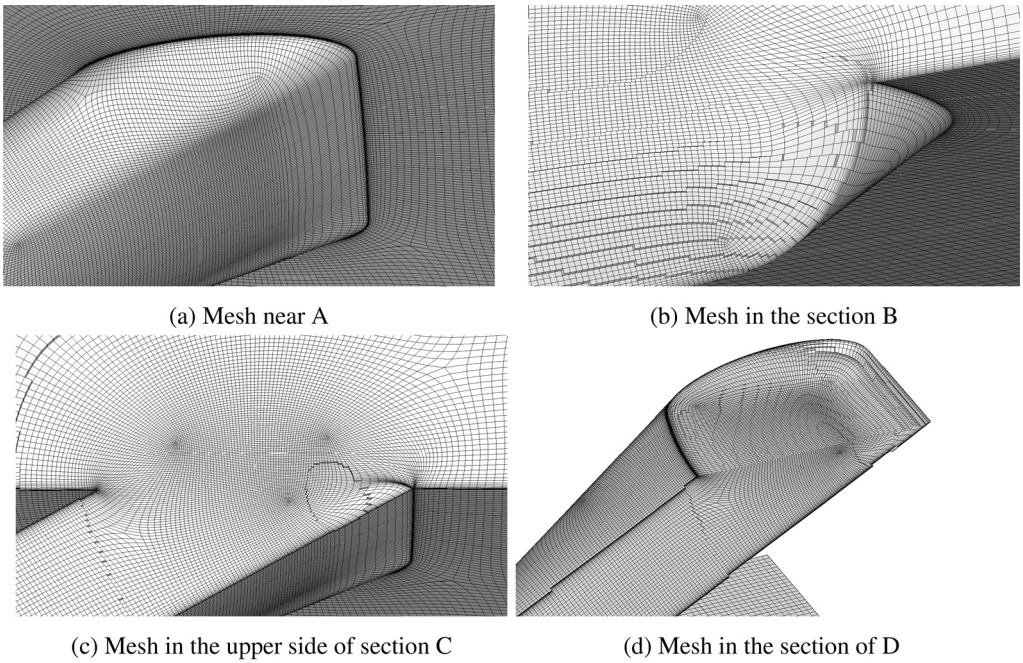

Fig. 3. Details of fan-shaped cooling hole mesh.

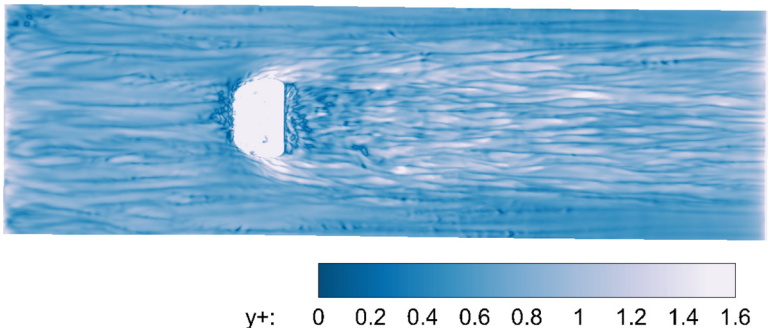

Fig. 4. y^+ contour at the flat plat surface of fan-shaped film cooling mesh.

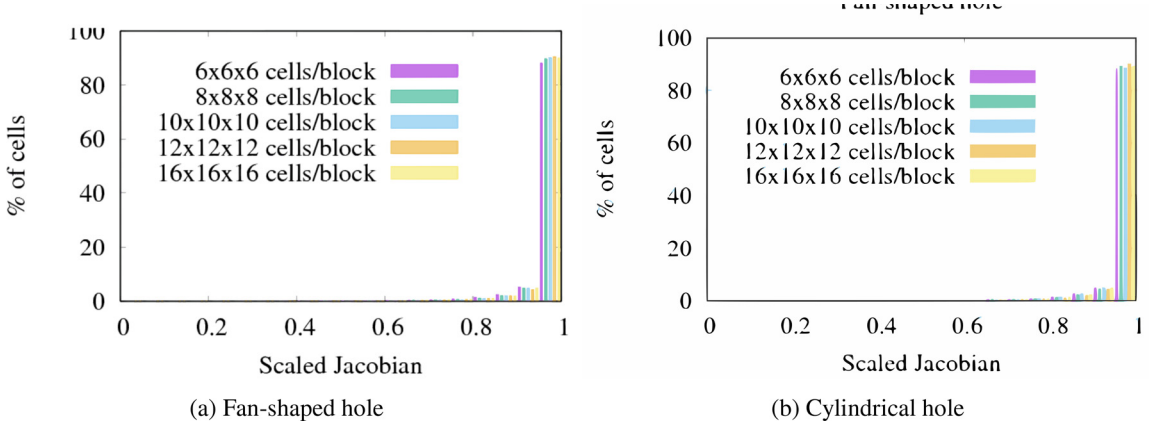

Fig. 5. Independence of grid quality on block cell count: (a) fan-shaped hole, (b) cylindrical hole.

chosen for a series of simulations to obtain discharge coefficients (see definition in [20]). The mesh of $16 \times 16 \times 16$ cells per block is used for obtaining film cooling effectiveness and turbulence statistics (Favre-averaged velocity profiles, Reynolds stresses profiles and turbulent heat flux profiles). It is also used to capture the turbulence structures in the coolant mixing process and the interaction between the coolant and the mainstream. Such task allocations are adopted for the consideration of minimum computational resources and time costs.

2.3. LES platform

A home-grown CFD code 'H4X' is used for LES simulations to solve the Navier-Stokes equations. The governing equations are

shown in Eq. 1:

$$\begin{aligned}
&\frac{\partial \rho}{\partial t}+\frac{\partial \rho u_j}{\partial x_j}=0\\
&\frac{\partial \rho u_i}{\partial t}+\frac{\partial \rho u_i u_j}{\partial x_j}+\frac{\partial p}{\partial x_i}=\frac{\partial \sigma_{ij}}{\partial x_j}\\
&\frac{\partial \rho E}{\partial t}+\frac{\partial (\rho E+p)u_j}{\partial x_j}=\frac{\partial \sigma_{ij}u_i}{\partial x_j}-\frac{\partial}{\partial x_j}q_j
\end{aligned} \tag{1}$$

The code adopts an implicit LES based on the finite volume approach for the numerical solution of conservation laws. All variables are stored at the cell center. Fluxes are evaluated at cell interfaces. Flow variables are extrapolated to the cell interfaces using the third-order limiter of Čada and Torrilhon [27]. The limiter is applied to the characteristic variables. For the purpose of applying slope limiters, the gradients are obtained using a weighted least squares method. The stencil of the gradients is biased locally by removing contributions from the state of the flow on the opposite side of the interface. The inviscid fluxes are evaluated using Roe's Riemann solver. The resulting scheme has a biased three-point stencil and is formally third-order accurate away from discontinuities and local extrema. The viscous fluxes are evaluated using unbiased least square gradients. The state of the flow used to evaluate transport properties is obtained by linear interpolation between the two cells sharing the interface. The resulting scheme for the viscous fluxes is centered and is formally second-order accurate.

The solution is advanced in time by using a third-order Runge-Kutta scheme. The scheme requires three flux evaluations and four updates for each time step. The CFL limit for the stability of the Runge-Kutta scheme is approximately 0.8, but a lower value is generally adopted during computations.

The three walls attached to the cooling hole (the bottom wall in the main channel, the top wall in the coolant channel, and the wall of the cooling hole) are handled by the non-slip adiabatic wall condition. The adiabatic thermal condition is applied to the temperature of these walls. The on-the-fly inlet boundary is set using a synthetic turbulence inflow generator described in Hao M, et.al [28]. The inflow generator is composed of two elements. One is a preliminary procedure that can infer realistic two-point covariance tensors from readily available data (e.g. freestream velocity, boundary layer thickness, and turbulence intensity). The other is an efficient eigen-decomposition step of the two-point correlation tensor that determines a set of modes. The capability of the inflow generator in retaining realistic spatial and temporal correlations allows for the generation of a realistic turbulent boundary layer for the inlets of film cooling in LES. The boundary layer thickness and turbulent intensity match the experimental data, as these parameters are specified for the inflow generator. The outflows for both external and internal channels are dealt with by the unsteady non-reflecting boundary condition based on Thompson [29]. Periodic boundary conditions are imposed on the walls in the spanwise direction. The periodicity has already been set during the meshing procedure by matching the corresponding cells on attached boundaries, for which no additional interpolation is needed for data exchange between blocks attached to the same boundary edge. The top wall in the main channel and the bottom wall in the coolant channel are treated as far-field boundaries. The blowing ratio is matched by adjusting the mass flow rate at the inlet of the mainstream and at the inlet of the coolant channel. The multi-block structure facilitates the implementation of MPI for coarse grain parallelism when using domain decomposition, and the implementation of OpenMPI allows for the parallelism among blocks within each MPI rank. The computational simulations are carried out in parallel on 480 processors, and the time run for numerical simulations of each case is shown in Table 2.

At the start of each computation, LES is run for around five flow-through times to eliminate the initial transient effects. Following that, statistics are collected for at least ten flow-through times for each case. Both integral quantities (running average of the mass flow rates) as well as variations in the profiles of velocity and Reynolds stress are monitored. In the last 10 flow-through times, all cases show below 2% variations. The CFL number is kept as 0.8.

3. Validation

3.1. Discharge coefficients

The discharge coefficient is one of the key parameters during both the design and the analysis of the cooling system. One reason is that the relation between the mass flow rate and the pressure drop of film cooling holes can be represented through the discharge coefficient C_D. This means that for a given coolant flow rate requirement, C_D determines the pressure margin. Another reason is that the discharge coefficient is related to the ratio between the nominal passage area and the area of the *vena contracta*. The definition of C_D is the ratio of the actual mass flow rate to the ideal mass flow rate through the hole. The ideal mass flow rate is obtained with the assumption of a one-dimensional and isentropic expansion from the total pressure in the plenum to the static pressure in the mainstream at the hole exit referring to [13], as

$$C_D=\frac{\dot{m}_c}{p_{tc}\left(\frac{p_m}{p_{tc}}\right)^{\frac{k+1}{2k}}\sqrt{\frac{2k}{(k-1)RT_{tc}}\left(\left(\frac{p_{tc}}{p_m}\right)^{\frac{k-1}{k}}-1\right)}\frac{\pi}{4}D^2} \tag{2}$$

Fig. 6 compares the C_D result with published experimental data [13] for the fan-shaped hole and the cylindrical hole. C_D is plotted versus the pressure ratio at three sets of operating conditions in an array of two main channel Mach numbers ($Ma_m = 0.6, 0.3$), one coolant passage Mach number ($Ma_c = 0.0$), and two orientation angels ($\beta = 0, 90^\circ$), The plateau value of $C_D = 0.8$ for the fan-shaped hole and $C_D = 0.75$ for the cylindrical hole are observed in the region of high-pressure ratio, regardless of Ma_m, which matches well the experiment. The numerical results and experimental data of discharge coefficients match very well in the larger pressure ratio region. The small difference between the numerical results and experimental data in the low-pressure ratio is observed because in LES simulations the Ma_c is not completely adjusted to zero for the purpose of letting the flow go through the coolant channel. This effect is more prominent in lower Ma_m conditions where the *vena contracta* is more sensitive to the precise configuration of the inflow. In general, the comparison generally shows good agreement with the experimental data.

3.2. Favre-averaged velocity

Fig. 7 compares the streamwise component of the Favre-averaged velocity at three positions at $x/D = 0, 2, 10$. Fig. 9 compares the Favre-averaged streamwise velocity on the slice at $x/D = 4$. It reflects the lateral spreading of the jet velocity. The overall prediction of velocity profiles matches the measured data well.

The flow features at $x/D = 4$ are compared: half of the counter-rotating vortex pair (CVP) from the cylindrical hole and the laterally-spreading flow downstream the fan-shaped hole are correctly captured. Both the shape and position of corresponding con-

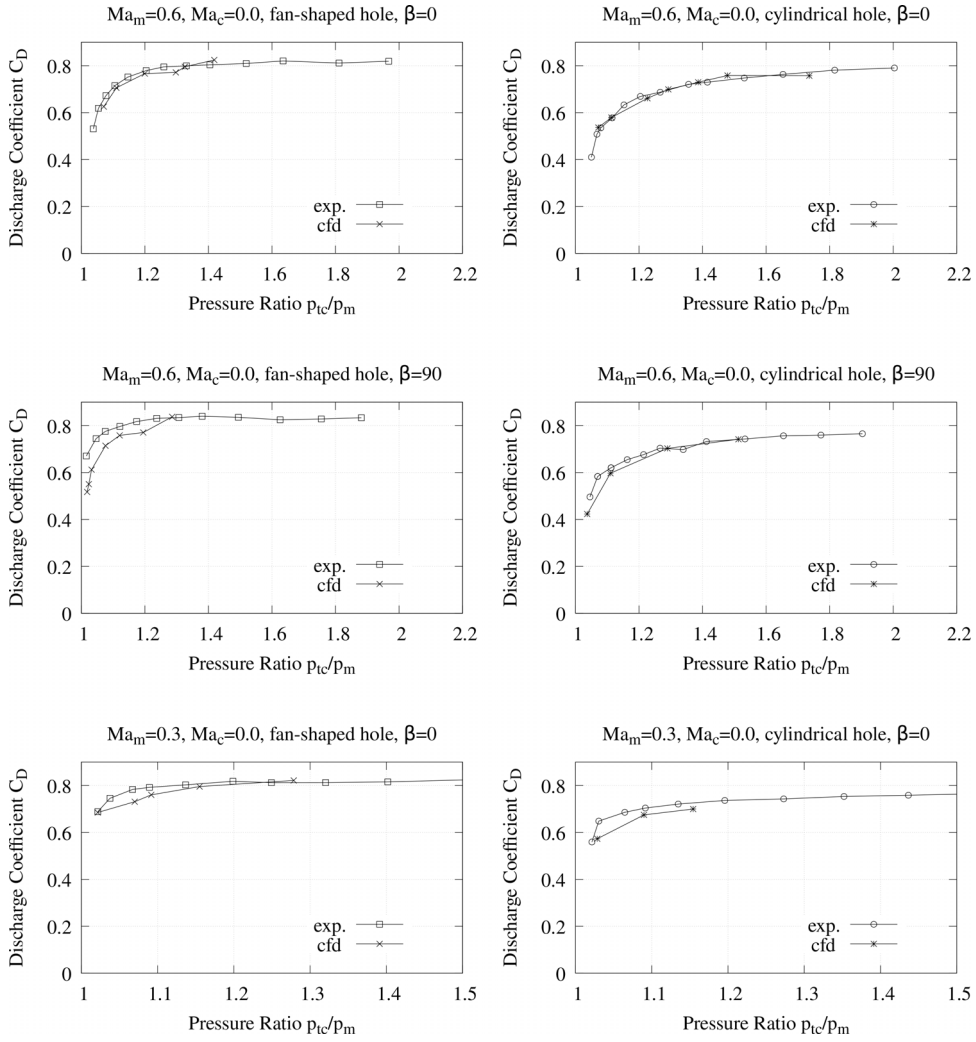

Fig. 6. Discharge coefficient for the cylindrical hole and the fan-shaped hole on three sets of operating conditions.

tour levels from LES predictions match fairly well with the measured data.

3.3. Turbulence intensities

Fig. 8 shows the turbulence intensity downstream of the cylindrical hole. A good comparison with the experimental profile is shown, with the matching shape of the u_{rms}/U_0 profile and an overprediction of less than 10% at the peaks. Fig. 10 compares the turbulence intensity contours on the slice at $x/D = 4$. It can reflect the lateral spreading of the turbulence of the jet. The overall prediction of the Reynolds stress matches the measured data well. The shape and position of the jet turbulence intensity match the measured data of both cooling holes.

3.4. Effectiveness

Fig. 11 shows the comparison of film cooling effectiveness downstream of the hole in the mainstream channel. Both the level and the trend of film cooling effectiveness match well for a range of blowing ratios and for the two studied hole types.

Overall, the validation has given this study confidence that the simulations in this study can reproduce the main features of experimental flows, in terms of the flow distribution, the coolant distribution, and the structure of turbulence.

4. Results and discussion

4.1. Favre-averaged velocity

Figs. 12 and 14 show the normalized Favre-averaged velocity profiles vs y/D downstream of the film cooling hole in the fan-shaped cases and in the cylindrical cases, respectively. The Favre-averaged velocity is normalized by the freestream velocity. In Fig. 12, the trajectory of the jet in the fan-shaped cases can be inferred. The main effect of the blowing ratio is to modify the location and the spreading rate of the jet. In the fan-shaped film, the jet is never lifted off. So the velocity defect caused by the jet is mostly confined below $y/D = 1$. Along the centerline ($z/D = 0$), the edge of the jet starts from between $0.8D$ and $1.0D$ at $x/D = 2$, depending on the blowing ratio, and it gradually grows as the flow evolves downstream. $z/D = 1.5$ is also examined in the fan-shaped hole cases to illustrate the edge of the film. Due to the shape of the jet, $z/D = 1.5$ presents velocity profiles thinner than those at $z/D = 0$. It also shows that the velocity profiles at $x/D = 5, 10, 15$ have the same shape. This suggests that after $x/D = 5$, the jet has become self-similar.

In order to test this hypothesis, Fig. 13 is shown to present the Favre-averaged velocity defect vs y/δ_{99} on the centerline of the fan-shaped hole. The Favre-averaged velocity defect is defined as $1 - U/U(\delta_{99})$ where $U(\delta_{99})$ is 99% of the freestream velocity. It is

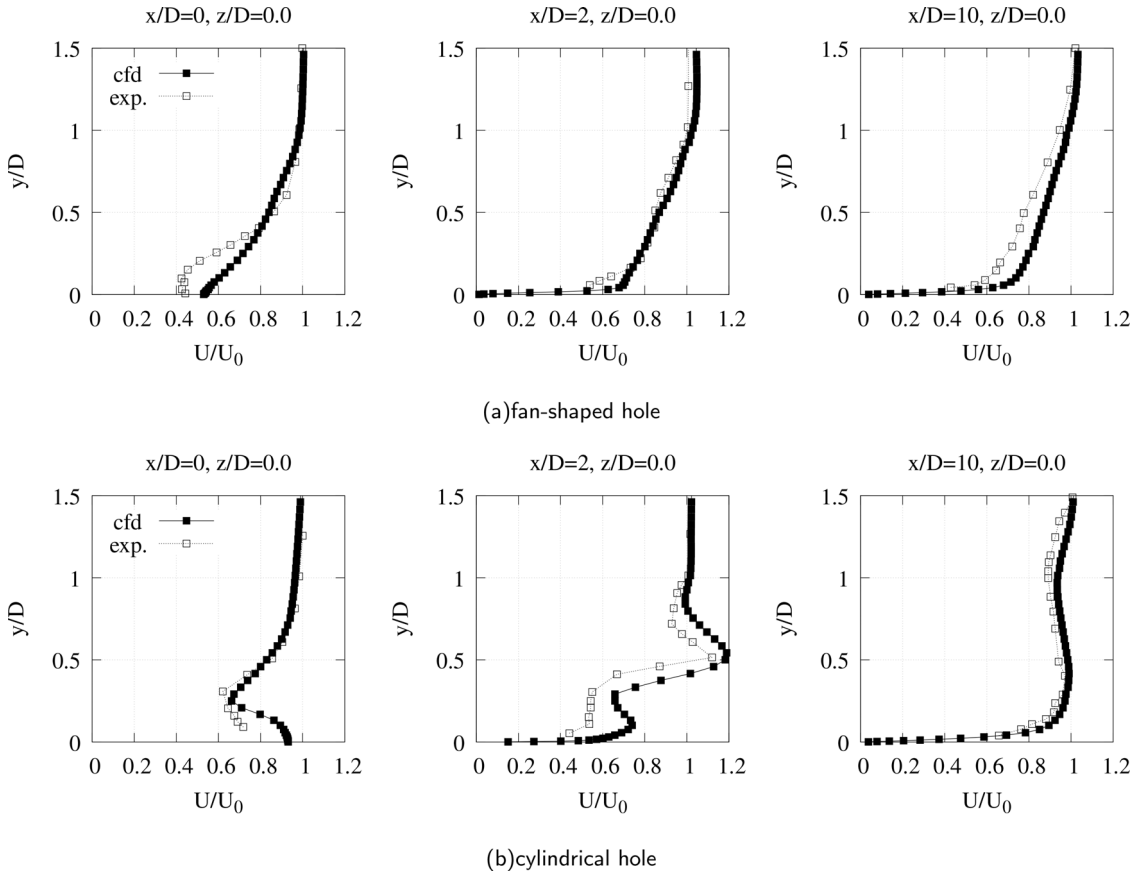

Fig. 7. Favre-averaged steamwise velocity profiles at (i)$x/D = 0$, (ii)$x/D = 2$, (iii)$x/D = 10$.

normalized by the velocity defect at the core of the jet H, which is evaluated as the velocity defect at the height of $\delta_{99}/2$ according to [30], shown in Eq. 3. The idea comes from the fact that δ_{99} is the local boundary layer height and it is modified by the presence of the jet.

$$H = 1 - \frac{U(\delta_{99}/2)}{U(\delta_{99})} \tag{3}$$

Fig. 14 indicates the trajectory of the jet downstream of the film cooling hole in the cylindrical cases. The centreline profiles are examined on $z/D = 0$, while the profiles on the edge of the film are examined on $z/D = 0.5$. In the cylindrical hole cases: at $M = 0.5$, the coolant is confined within half the diameter of the wall starting from $x/D = 2$ and gradually mixes with the mainstream as it travels downstream; at $M = 1.0$, the freestream flow is entrained between the jet and the wall starting from $x/D = 2$, with the jet centerline approximately located half diameter from the wall; at $M = 1.5$, the jet is lifted off, and the freestream fluid comes as the flow next to the wall.

Fig. 15 shows the Favre-averaged velocity defect profiles vs y/δ_{99} downstream of the film cooling hole in the cylindrical cases. It uses the same definition and normalization of Favre-averaged velocity defect as Fig. 13. In Fig. 15: at $M = 0.5$, the jet has become self-similar after $x/D = 5$, because the coolant is not lifted off yet; at $M = 1.5$, the jet has become self-similar after $x/D = 5$, because the coolant is mostly lifted off; at $M = 1.0$, the jet doesn't present the self-similarity after $x/D = 5$, because the coolant is partially entrained. $M = 1.0$ is therefore an intermediate blowing ratio.

4.2. Favre-averaged non-dimensional temperature

Fig. 16 shows the non-dimensional profiles of Favre-averaged temperature for the fan-shaped film. In the fan-shaped hole cases (shown in Fig. 16), at the exit of the fan-shaped films ($x/D = 2$), the non-dimensional temperature near the wall has the value corresponding to the coolant stream. Therefore, the flow near the wall at the exit of the hole must be formed by an unmixed coolant. As the coolant fluid moves downstream, it gradually mixes and the non-dimensional temperature near the wall rises. Fig. 17 shows the temperature deficit profiles in fan-shaped films. The non-dimensional temperature deficit vs y/δ_{99} is presented on the centerline and on the film edge. The Favre-averaged temperature deficit ([31]) is defined as $1 - T/T_{99}$ where T_{99} is the temperature at δ_{99}. It is normalized by the Favre-averaged temperature deficit at the core of the jet Θ,

$$\Theta = \frac{T_m - T(\delta_{99}/2)}{T_m - T_{tc}} \tag{4}$$

which is evaluated as the Favre-averaged temperature deficit at $\delta_{99}/2$. Fig. 17 shows that the temperature deficit profiles are self-similar with the exception of the lowest blow ratio in fan-shaped films. This finding confirms the behavior already observed on the velocity profiles.

Fig. 18 shows the non-dimensional profiles of Favre-averaged temperature for the cylindrical hole. At the lowest and highest blowing ratios, the profiles downstream show similarities, while at $M = 1.0$, the profiles overall do not show similar behaviors. At $M = 1.0$, the top part of the profiles shows similarity, but the lower part never does. The reason for this is that the jet is about to lift

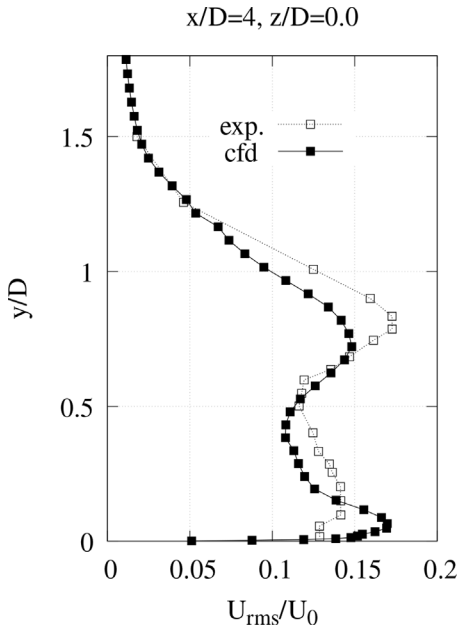

Fig. 8. Comparison of u_{rms} at $x/D = 4$ of cylindrical hole with those from experimental data [12].

off. The similarity patterns are shown in the temperature deficits (in Fig. 19). Fig. 19 shows that the temperature deficits at both $M = 0.5$ and $M = 1.5$ collapse from $x/D = 5$ because either they have not lifted off or lifted off too early, while the temperature deficits at $M = 1.5$ do not show a self-similarity pattern below $y/\delta_{99} = 0.5$.

Table 3 shows the values of the temperature deficit at the height of $\delta_{99}/2$, which corresponds to the height of the jet core. Table 3 can be analyzed by taking ratios of velocity defects at $x/D = 2$ to the corresponding values at $x/D = 15$. The same process can be applied to temperature deficits. In this way, estimates of the Favre-averaged decay rates of velocity and temperature deficits can be obtained. The decay rates of quantities such as adiabatic effectiveness downstream of isolated films are fundamental quantities in correlations. The decay rates are direct results of the rates at which momentum and energy are transferred between the jet and the hot stream and within the jet.

In the fan-shaped cases, the decay rates of the velocity defects on the centerline are around 2 with the lowest value 1.87 at $M = 1$, while those values on the edge of the jet are 2 at $M = 0.5$ and increase to 2.4 at $M = 1.5$. The decay rates of the temperature deficit on the centerline are around 3 with the lowest value of 2.44 at $M = 1$, while those values on the edge of the jet are around 3 starting from 2.5 at $M = 0.5$. There are two sets of phenomena determining the decay rates. At the centerline the distribution of the coolant evolves under the action of two counter-rotating vortices which draw hot air under the jet and move the cold air into a thinner layer in the top half of the jet; all the while the jet mixes with its surroundings. The quicker decay of the temperature deficit is due partly to the redistribution of the coolant within the jet and partly to turbulent mixing, which progresses at different rates for momentum and energy.

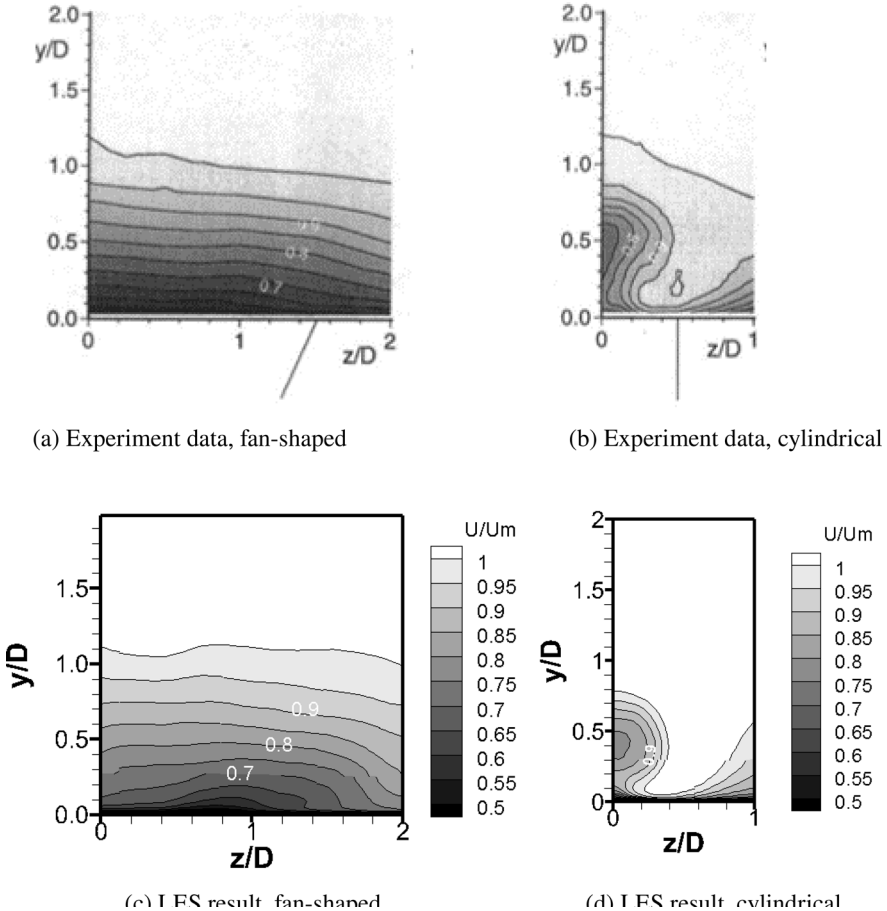

(a) Experiment data, fan-shaped

(b) Experiment data, cylindrical

(c) LES result, fan-shaped

(d) LES result, cylindrical

Fig. 9. The comparison of time-averaged streamwise velocity contours at $x/D = 4$ between experimental data from Thole et al. [12] and LES results in the fan-shaped and the cylindrical film.

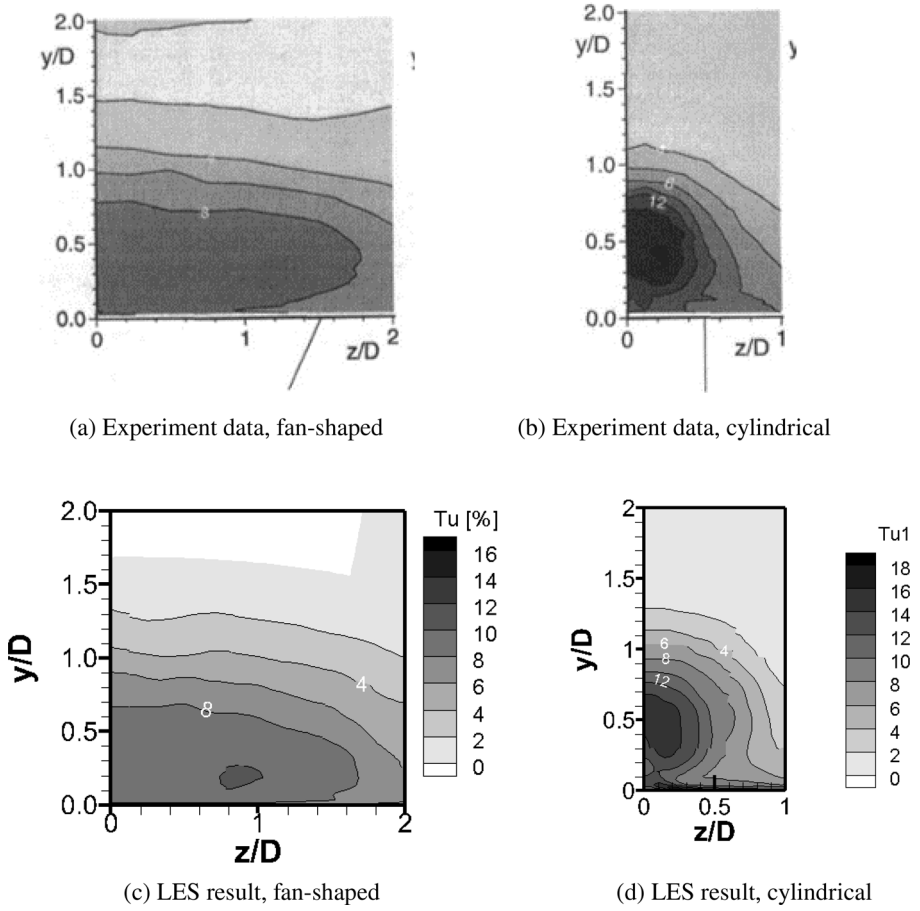

(a) Experiment data, fan-shaped (b) Experiment data, cylindrical

(c) LES result, fan-shaped (d) LES result, cylindrical

Fig. 10. The comparison of turbulence intensity contours at $x/D = 4$ between experimental data from Thole et al. [12] and LES results in the fan-shaped and cylindrical film cooling.

Table 3
Favre-averaged velocity and temperature defects on the centreline and on the edge of the jet.

		Fan-shaped				Cylindrical			
		$z/D = 0$		$z/D = 1.5$		$z/D = 0$		$z/D = 0.5$	
	x/D	V	T	V	T	V	T	V	T
0.5	2	0.229	0.114	0.137	0.026	0.463	0.316	0.291	0.164
	15	0.100	0.033	0.068	0.010	0.112	0.042	0.94	0.035
1.0	2	0.284	0.204	0.204	0.100	0.386	0.389	0.271	0.301
	15	0.151	0.084	0.093	0.032	0.157	0.097	0.122	0.084
1.5	2	0.304	0.259	0.219	0.145	0.308	0.413	0.117	0.369
	15	0.151	0.084	0.090	0.048	0.135	0.120	0.082	0.094

In the cylindrical film, the decay rates of the velocity defects on the centerline decrease from 4 at $M = 0.5$ to 2.3 at $M = 1.5$, while those values on the edge of the jet decrease from 3.1 at $M = 0.5$ to 1.4 at $M = 1.5$. The decay rates of the temperature deficit on the centerline decrease from 7.5 at $M = 0.5$ to 3.4 at $M = 1.5$, while those values on the edge of the jet decrease from 4.7 at $M = 0.5$ to below 4 at $M = 1.0$ and at $M = 1.5$. At the lowest blowing ratio, the coolant jet mixes rapidly with the hot stream, and the velocity defect and temperature deficit decay correspondingly fast. At higher blowing ratios, the jet starts lifting from the wall and mixes at a slower rate with its surroundings, explaining the lower values of the mixing rates. The decay of velocity defects at the edge of the jet becomes slower than that at the centerline, as is the case in isolated turbulent jets [32]. The difference in decay rates of the velocity defect and temperature defects is a macroscopic consequence of the turbulent Prandtl number deviating from unity. It is known that the turbulent Prandtl number is in fact a varying quantity throughout boundary layers and shear flows. The variability of the turbulent Prandtl number, together with the way the flow is redistributed within the film jet, also causes temperature and velocity defects to decay at different rates in different parts of the jet.

4.3. Reynolds stress

Energy-carrying structures contribute the most to the Reynolds stresses. Therefore, an inspection of these structures can provide indications of the origin and behavior of Reynolds stresses.

Fig. 20 shows the density gradient on the median $x - y$ plane, capturing the size and distribution of energy-carrying structures, which are compared between different blowing ratios. In all cases, the high-density gradient region originates from a Kelvin-Helmholtz instability induced by a shear layer that appears at the windward side of the hole exit.

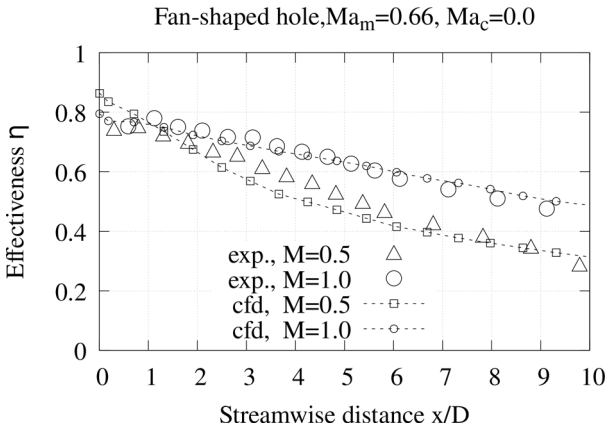

Fig. 11. Comparison of the effectiveness of fan-shaped holes with those from experimental data [13].

For the fan-shaped hole at $M = 0.5$ (as seen in Fig. 20(a)) and $M = 1.0$ (as seen in Fig. 20(b)), the shear layer from the windward side of the hole exit falls at the leeward edge of the hole exit, interacts with the boundary layer, and lifts up hairpin vortices from the leeward edge of the hole exit, which evolve into the hairpin packets downstream. The size of hairpin vortices doubles going from $M = 0.5$ to $M = 1.0$, as evidenced by the second hairpin marked in both cases. The vortices are attached to the wall surface in both these two cases. However, at $M = 1.5$ (as seen in Fig. 20(c)) in the fan-shaped case, the shear layer from the windward side of the hole lifts up until it interacts directly with the boundary layer above the mainstream channel surface. This leads to the appearance of hairpin vortices at $x/D = 2.5$. The behavior of the shear layer in the cylindrical cases at all the blowing ratios is correspondingly similar.

The height of vortices arrives at the highest at $x/D = 10$ of the cylindrical hole case at $M = 1.5$, and the height is around 3.7δ. It is also worth mentioning that with the increasing blowing ratio, the number of small-scale turbulent structures increases, giving rise to better cooling film coverage due to an improved vortex shedding frequency. This can be more obvious for the cylindrical cases because the significantly increased vortex shedding inside the cooling hole is a source of turbulence onto the mainstream channel surface, while the interaction between coolant and mainstream dominates the corresponding source in the fan-shaped cases. The size of these hairpin vortices scales with the thickness of the wall jet. The number of energy-carrying structures that can be accommodated by the jet scales with its width. This could be found in similar instantaneous vortex structures in the $y - z$ plane (not shown here).

The boundary layer turbulence intensity at the inlet is 1.5%, and the boundary layer thickness is $0.5D$, as shown in Table 2. The turbulence intensity from the film hole varies from 1% at $M = 0.5$ to 4% at $M = 1.5$. The highest value of $< u'u' >$ is located across the mixing layer between the air injected into the flow near the upstream edge of the film and the freestream. This observation holds for both fan-shaped and cylindrical films, as indicated in Fig. 20.

Fig. 21 compares the scaled normal stress along a series of streamwise positions at different blowing ratios. In the fan-shaped film, at $M = 0.5$, the peak of normal stresses is below the edge of the incoming boundary layer, while at $M = 1.0$ and $M = 1.5$, the peak of the normal stresses of the jet is above the edge of the boundary layer. In the cylindrical film, at $M = 0.5$, the jet is fully confined within the boundary layer, while at $M = 1.0$ and $M = 1.5$, part of the jet is located above the boundary layer.

Figs. 22, 23, and 24 compare the three components of Reynolds normal stresses. Figs. 22, 23, and 24 show the fan-shaped film at different blowing ratios, while Figs. 22b, 23 b, and 24 b show the cylindrical film cases at different blowing ratios. In the fan-shaped films, there is a clearly recognizable two-layer structure in the Reynolds normal stresses. The two main components of the flow are a boundary layer in the proximity of the wall and a shear layer in the upper part of the jet. Both layers spread gradually as the flow develops downstream. The part of the flow behaving as a developing boundary layer extends vertically up to approximately $y/D = 0.2$ to $y/D = 0.4$. The normal stresses are relatively flat in

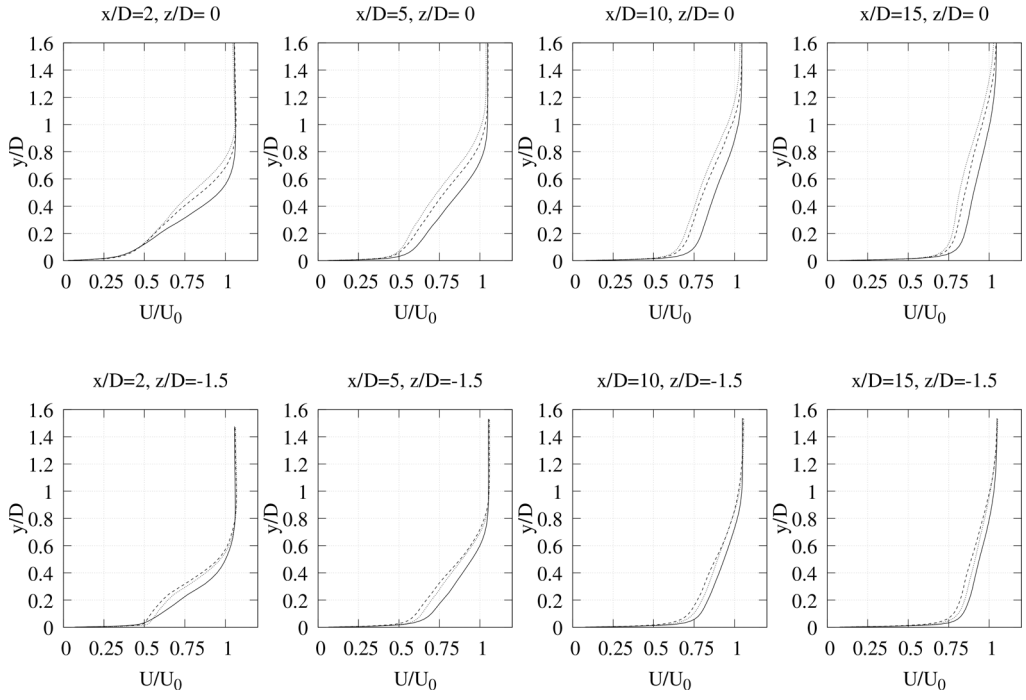

Fig. 12. The distribution of Favre-averaged streamwise velocity profiles at different locations downstream of the fan-shaped hole. Solid line: M=0.5; dash line: M=1.0; dot line: M=1.5.

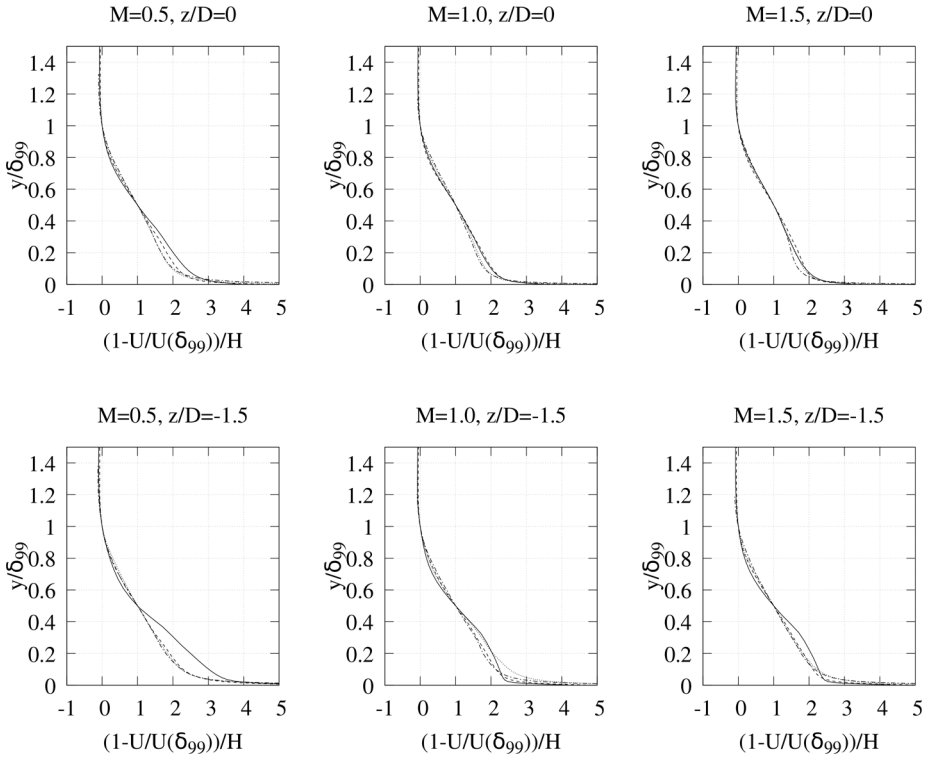

Fig. 13. Normalized Favre-averaged velocity defect downstream of the fan-shaped hole. Solid line: $x/D = 2$, dash line: $x/D = 5$, dot line: $x/D = 10$, dash-dot line: $x/D = 15$.

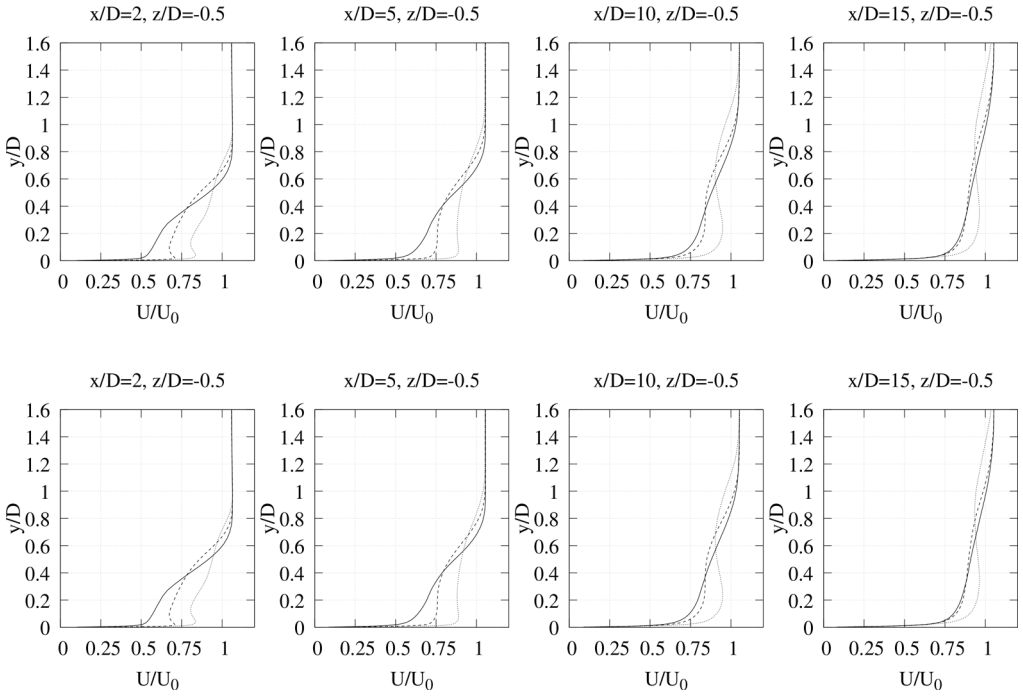

Fig. 14. The distribution of Favre-averaged streamwise velocity profiles at different locations downstream of the cylindrical hole. Solid line: M=0.5; dash line: M=1.0; dot line: M=1.5.

this part of the flow. The turbulence in the fan-shaped film is more isotropic in the near-wall region. The anisotropy in the cylindrical cooling film is caused by the hairpin vortices being few and mostly aligned in the direction orthogonal to the flow. By contrast, hairpin vortices are smaller and more numerous in the fan-shaped film.

Fig. 25 shows the distribution of Reynolds shear stresses in two types of films. Fig. 25a compares three fan-shaped hole cases at different blowing ratios. Fig. 25b compares three cylindrical hole cases at different blowing ratios. The comparison in this section is arranged to explain separately the behavior of the Reynolds stresses within a short distance from the film (near field) and at a longer distance (far field).

The near-field flow is analyzed at $x/D = 2$ and 5, and it is dominated by the boundary layer in the mainstream channel and by the properties of the turbulence established within the film. In fan-shaped films, at $M = 0.5$, the Reynolds shear stress is negative

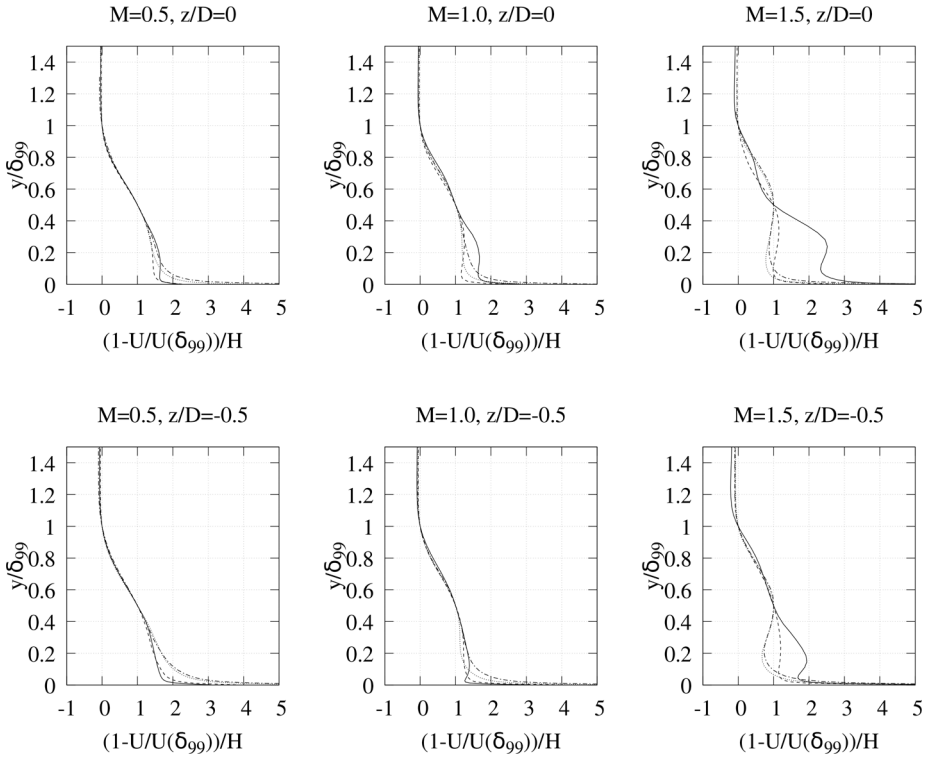

Fig. 15. Normalized Favre-averaged velocity defect downstream of the cylindrical hole. Solid line: $x/D = 2$, dash line: $x/D = 5$, dot line: $x/D = 10$, dash-dot line: $x/D = 15$.

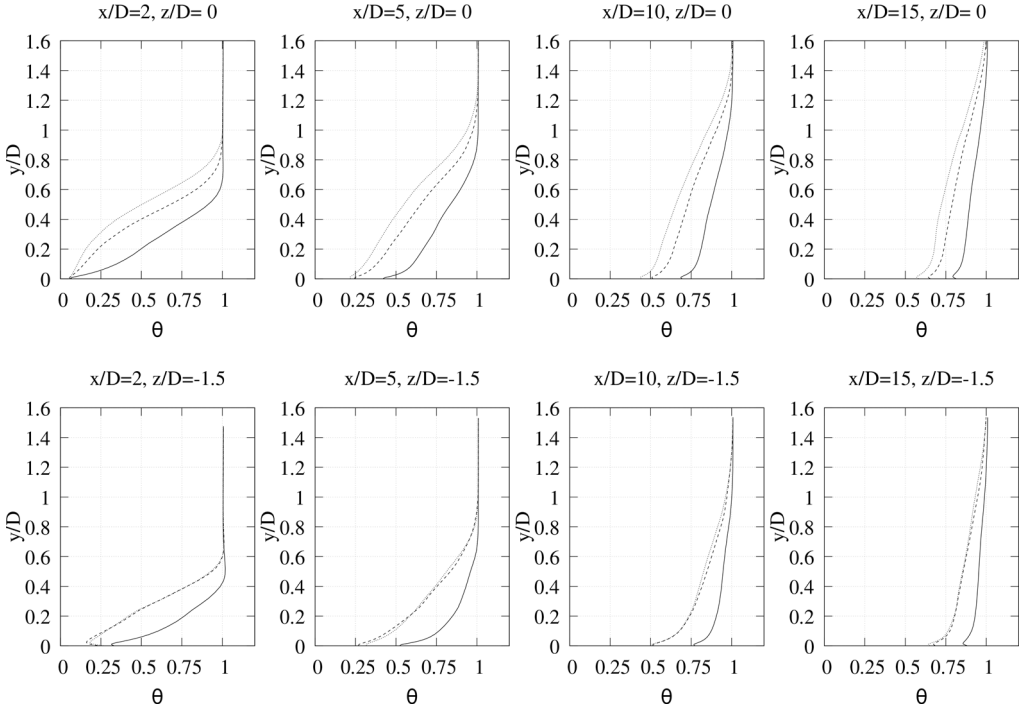

Fig. 16. The distribution of Favre-averaged temperature profiles at different locations downstream of the fan-shaped hole. Solid line: M=0.5; dash line: M=1.0; dot line: M=1.5.

everywhere as long as it deviates from zero. Momentum is transferred from the freestream to the coolant jet, and from the coolant jet towards the wall (negative peaks at $y/D = 0.1$ and $y/D = 0.6$). At $M = 1.0$ and $M = 1.5$, momentum is transferred from the jet to the wall (negative peaks) and from the freestream to the jet. In cylindrical films, at $M = 0.5$, momentum is transferred from the jet to the freestream (positive peak at $y/D = 0.5$) and from the jet to the wall. The level of the Reynolds shear stress for cylindrical cases is low in proximity to the wall. At $M = 1.0$ and $M = 1.5$, momentum transfer in cylindrical films takes place in the same direction as in fan-shaped films. However, in cylindrical cases, the locations where peak stresses are attained are further away from the wall. As an example, for $M = 1.0$, momentum is transferred from the jet to the wall (negative peak at $y/D = 0.3$) and from the

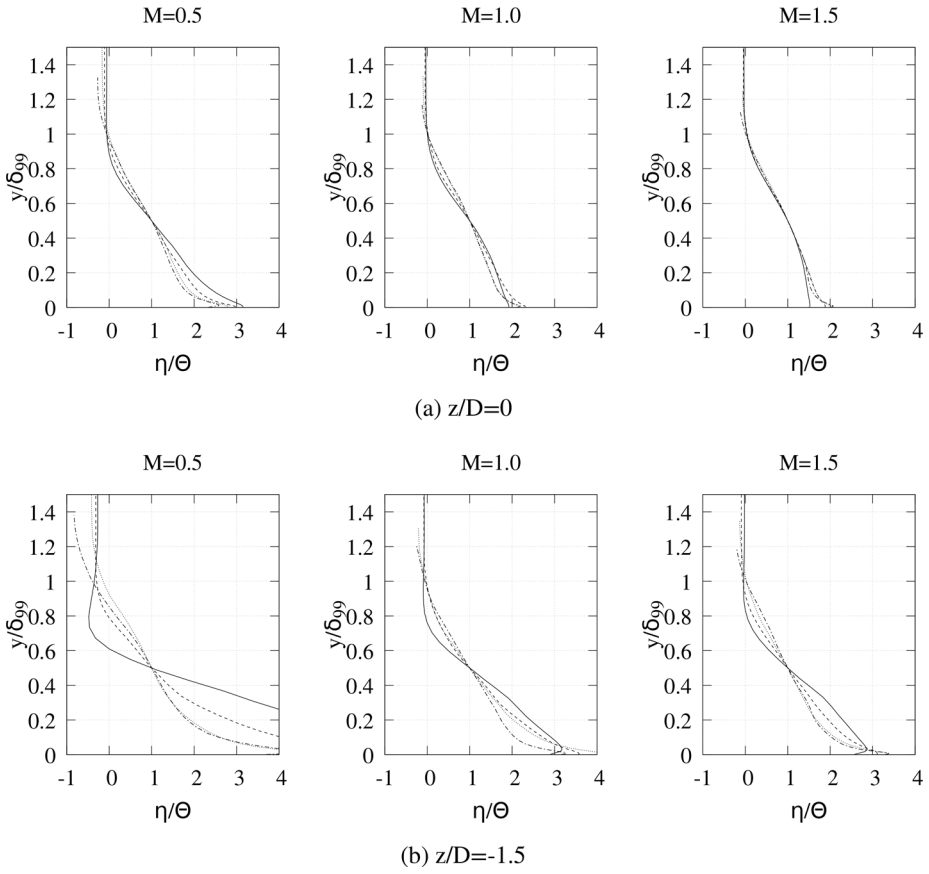

Fig. 17. Non-dimensional Favre-averaged temperature deficit downstream of the fan-shaped hole. Solid line: $x/D = 2$, dash line: $x/D = 5$, dot line: $x/D = 10$, dash-dot line: $x/D = 15$.

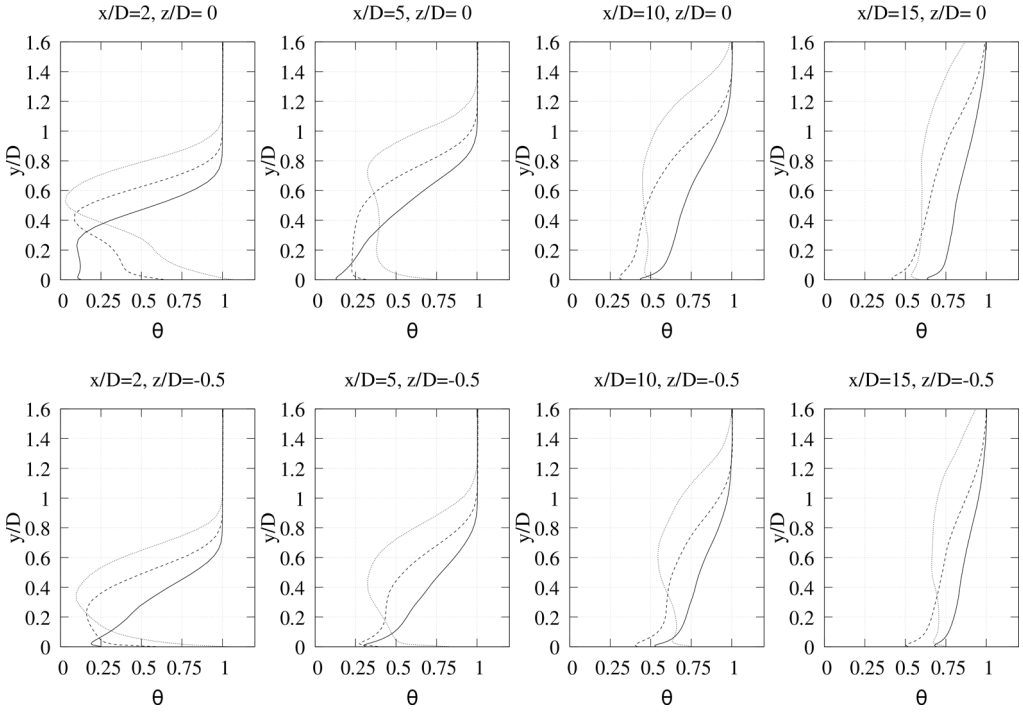

Fig. 18. The distribution of Favre-averaged temperature profiles at different locations downstream of the cylindrical hole. Solid line: M=0.5; dash line: M=1.0; dot line: M=1.5.

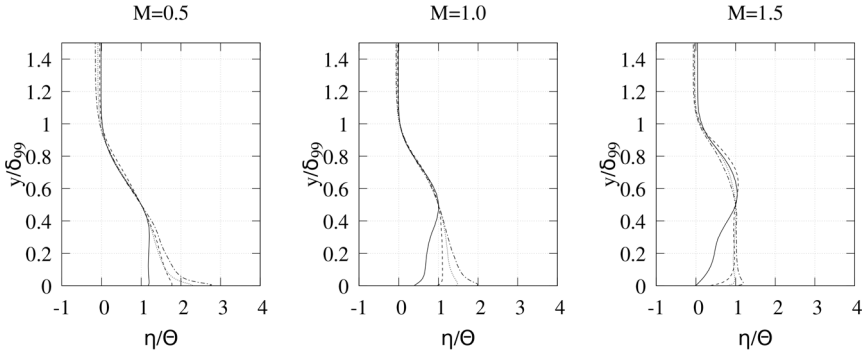

(a) $z/D = 0$

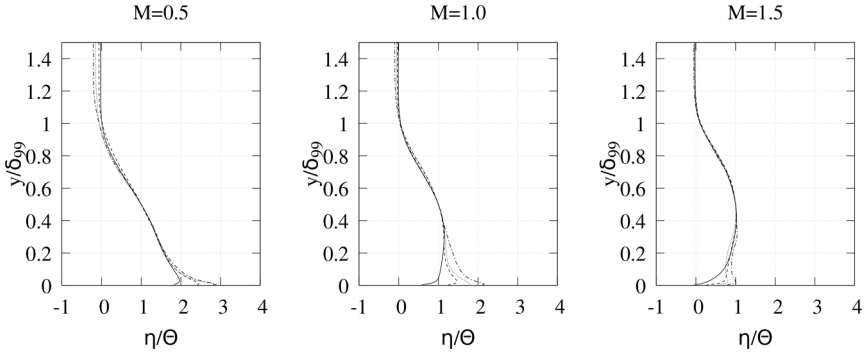

(b) $z/D = -0.5$

Fig. 19. Non-dimensional Favre-averaged temperature deficit downstream of the cylindrical hole. Solid line: $x/D = 2$, dash line: $x/D = 5$, dot line: $x/D = 10$, dash-dot line: $x/D = 15$.

jet to the freestream (positive peak at $y/D = 0.8$). At $M = 1.5$, momentum transfer is similar but stronger; momentum is transferred from the jet to the wall (negative peak at $y/D = 0.35$) and from the jet to the freestream (positive peak at $y/D = 0.8$).

Far-field flow is analyzed at $x/D = 10$ and 15. In the far field, the properties of turbulence are determined by the mixing between the jet and surrounding flow. A peak next to the wall is due to the developing boundary layer, and a relatively flat region that corresponds to the core of the jet. For the fan-shaped films, only at $M = 0.5$, the jet is still confined in the original boundary layer; for the other two blowing ratios, the jet grows to a height larger than the original boundary layer thickness. For the cylindrical films, at $M = 0.5$, the jet is still attached to the wall, whereas at $M = 1.0, 1.5$, the jet is about to be lifted off. Furthermore, the jet produced by the cylindrical films stands at a greater distance from the wall, compared to those produced by the fan-shaped films at the same blowing ratios.

The existence of self-similarity properties in the Favre-averaged velocity and temperature profiles suggests that Reynolds stress profiles may also enjoy similarity properties. Figs. 22a, 23a and 24a normalize profiles of the normal Reynolds stress by the freestream velocity squared. Differently from Favre-averaged velocity and temperature profiles, the Reynolds stresses can only be considered to achieve near similarity in the first approximation using this scaling. In the far field ($x/D = 10, 15$), the observations apply to both the cylindrical and fan-shaped films.

At moderate blowing ratios ($M = 0.5, 1.0$), the normal Reynolds stresses in the fan-shaped film, are higher than the Reynolds stresses in the cylindrical film. At the highest blowing ratio, the cylindrical film has higher normalized intensities compared to the other cases. In both fan-shaped and cylindrical films, the normal stresses are nearly uniform throughout the jet.

In the cylindrical hole, the jet is lifted off, so there is turbulence created by the jet that interferes with the wall region. Therefore, no deficit appears in the wall stresses between the wall and the lower edge of the jet. The structure of the flow near the wall is dominated by the boundary layer growing under the jet. In the fan-shaped films, the jet is not lifted off, and the turbulence from the jet is present in the near-wall region. As a result, the shape of the Reynolds normal stress distributions in the far field of fan-shaped and cylindrical films are not very different. The effect of the blowing ratios is to move the peak of the normal stress distributions away from the wall. The higher the blowing ratio is, the further away the jet is from the wall. The part of the jet not influenced by the presence of the wall extends from $y/D = 0.2$ to the height between $y/D = 0.6$ and 0.8 for the fan-shaped hole and the height between $y/D = 1$ and 1.5 for the cylindrical hole. The normal stresses are relatively flat in this domain. The turbulence in the fan-shaped film is very isotropic in the near-wall region. The turbulent flow generated by the cylindrical film is isotropic. The position of the local maximum in the normal stresses shows that the jet produced by the cylindrical film stands downstream further away from the wall compared to the jet produced by a fan-shaped film of similar blowing ratios. However, the locations where peak stresses are attained are further away from the wall.

Figs. 26 and 27 show the Reynolds stresses scaled by the corresponding Reynolds stress components at the core of the jet vs the wall-normal distance from the core of the jet scaled by the distance between δ_{99} and the core of the jet, that is $(y - \delta_{99})/(\delta_{99} - \delta_{99/2})$. By using this scaling, a better demonstration of the self-similar pattern is discovered in each Reynolds stress component away from the wall in the far-field region. In the fan-shaped cases (in Fig. 26), the scaled $< u'u' >$, $< v'v' >$, $< w'w' >$ and $< u'v' >$

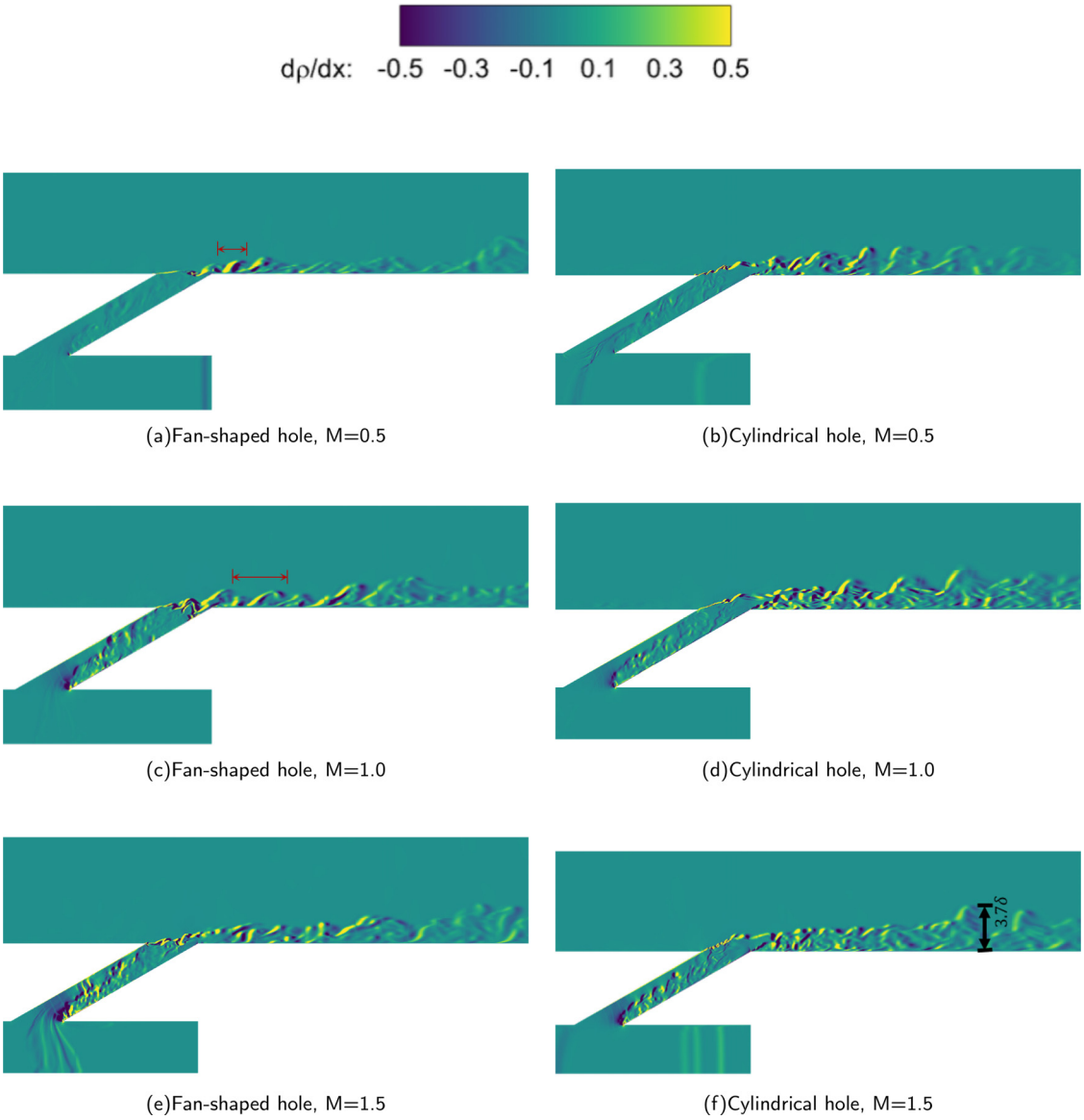

Fig. 20. Instantaneous snapshot of the density gradient.

at different blowing ratios collapse well above the core of the jet for the near-field region, and collapse well both above the core of the jet and near the wall for the far-field region. In contrast, for cylindrical cases(in Fig. 27), the scaled Reynolds stress components $< u'u' >$, $< v'v' >$, $< w'w' >$ and $< u'v' >$ exhibit larger differences among different blowing ratios in the near-field region. This is due to the varying flow mechanisms attached to the wall at different blowing ratios, as discussed previously. The scaled Reynolds stress components tend to collapse well above the core of the jet in the far-field region. Overall, the scaling analysis helps to highlight the self-similar nature of Reynolds stresses in the far-field region. However, the behavior of Reynolds stresses in the near-field region is more complex and depends on the blowing ratio and the geometry of the film.

4.4. Turbulent heat flux

Fig. 28 shows the distribution of turbulent heat flux along the wall-normal direction in two types of holes. The turbulent flux is defined as the Favre-averaged product of the velocity fluctuation and the non-dimensional temperature fluctuation. The definition of the non-dimensional temperature is shown below:

$$\theta = \frac{T - T_c}{T_m - T_{tc}} = 1 - \eta \tag{5}$$

The net heat flux on the wall must be zero due to the adiabatic wall condition, whereas the momentum flux on the wall is not zero because of friction. Therefore, the shape of the turbulent heat flux and the shape of the Reynolds stresses must be different next to the wall. However, away from the wall, the shape of the turbulent heat flux is identical to the shape of the Reynolds shear stresses (shown as in Fig. 25), apart from the sign. Comparing Figs. 28 and 25, the positions of the peaks of turbulent heat fluxes and Reynolds shear stress away from the wall are close. This applies to all three blowing ratios.

In the fan-shaped film as shown in Fig. 28a, at $M = 0.5$, the peak of turbulent heat flux is everywhere negative. At $x/D = 2$, heat is transferred from the freestream to the coolant jet, with a negative peak located at $y/D = 0.4$ on the centerline. This peak is identified as the upper edge of the jet. The direction of the heat

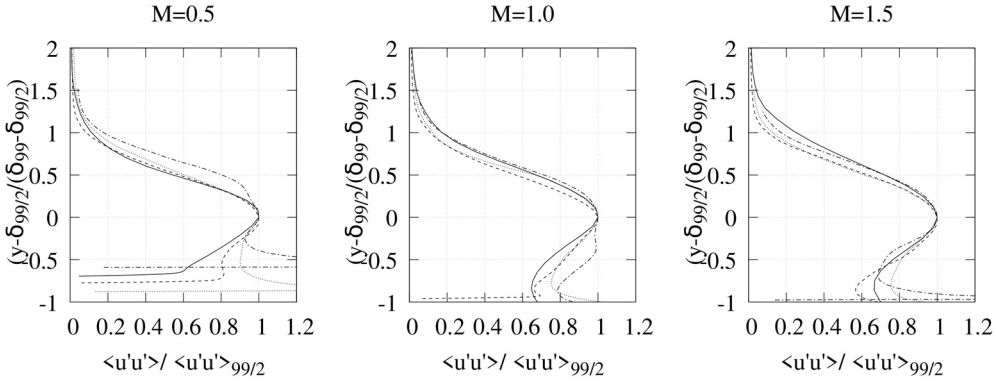

(a) Fan-shaped film

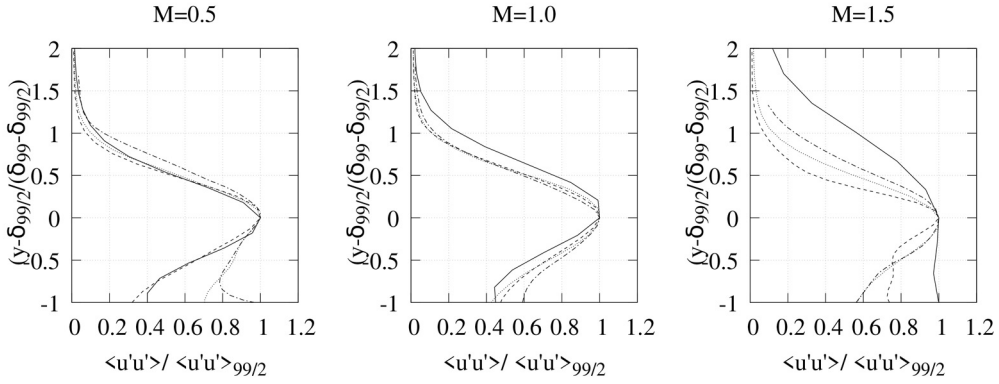

(b) Cylindrical film

Fig. 21. Profiles of the Reynolds normal stress $< u'u' >$ normalized by $< u'u' >$ at the core of the jet $\delta_{99}/2$ Solid line: $x/D = 2$, dashed line: $x/D = 5$, dot line: $x/D = 10$, dash-dotted line: $x/D = 15$.

flux at the upper edge of the jet is preserved as the flow develops downstream from $x/D = 5$ to $x/D = 15$. In all cases considered the temperature of the free stream is higher than the temperature of the coolant. Any mixing at the edge of the jet causes a turbulent heat flux from the free stream to the jet. This explains the negative sign of the turbulent heat flux at the edge of the jet. This situation should be contrasted with the change in the direction of the momentum flux, which is determined by the blowing ratio. The peak of turbulent heat flux is located further away from the wall as the blowing ratio is higher at each streamwise position. As an example, At $x/D = 2$ on the centerline, the peak of turbulent heat flux is located at $y/D = 0.5$ for the $M = 1.0$ case and at $y/D = 0.6$ for the $M = 1.5$ case. Similarly, the negative peak can be identified but with a smaller amplitude on the edge of the jet $z/D = -1.5$ of the fan-shaped film.

In the cylindrical film as shown in Fig. 28b, the negative peak can also be identified throughout the downstream flow domain at each blowing ratio, indicating the upper edge of the jet. As an example at $x/D = 2$ on the centerline of the cylindrical film, heat is transferred from the freestream to the jet with a negative peak at $y/D = 0.5$ for the $M = 0.5$ case, while for the $M = 1.0$ case and the $M = 1.5$ case, heat transfer takes place in the same direction with the negative peak located at $y/D = 0.6$ and $x/D = 0.8$, respectively. In addition, a positive peak of turbulent heat flux is also identified at a position lower than that of the negative peak. At $x/D = 2$ on the centerline, the positive peak is tiny for the $M = 0.5$ case, which is located at $y/D = 2$, but largest for the $M = 1.5$ case, which is located at $y/D = 0.35$. Both the positive and amplitude of the positive peak for the $M = 1.0$ case are in between. The positive peak disappears first in the lowest blowing ratio case till $x/D = 5$, then in the medium blowing ratio case till $x/D = 10$, and retains the longest distance at the highest blowing ratio as the jet goes downstream. This positive peak is identified as the lower side edge of the jet. The sign of the heat flux is determined to a large extent by the relative position of the coolant and the cold jet. The appearance of the positive peak in the cylindrical is because the jet is lifted from the wall and the hot air is drawn under the jet. This results in turbulent fluctuations in the area under the jet moving hot air upwards and cold air downwards, giving a net positive heat flux. Similarly, the patterns of the two peaks can be discovered but with smaller amplitudes on the edge of the jet $z/D = -0.5$ of the cylindrical film.

Fig. 29 shows turbulent heat flux in the wall-normal direction $< v't' >$ scaled by the corresponding turbulent heat flux at the core of the jet, vs the wall-normal distance from the core of the jet scaled by the distance between δ_{99} and the core of the jet, which is $(y - \delta_{99})/(\delta_{99} - \delta_{99/2})$. By using this scaling, a better demonstration of the self-similar pattern can be observed in the wall-normal component of the turbulent heat flux throughout the wall-normal distance for the fan-shaped films. For the cylindrical cases, the turbulent heat flux curves collapse well above the core of the jet, while the curve at the highest blowing ratio deviates. The curves close to the wall lack self-similarity. This shows that even when the flow mechanism is different, the self-similar pattern also exists

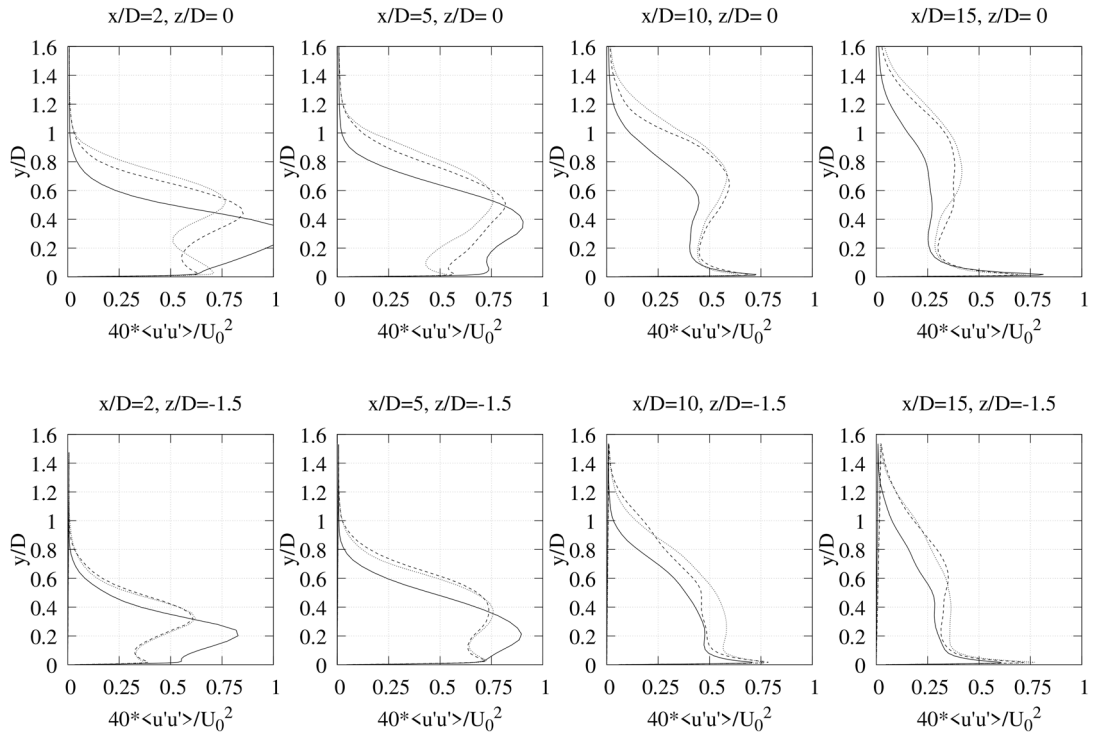

(a) Fan-shaped film

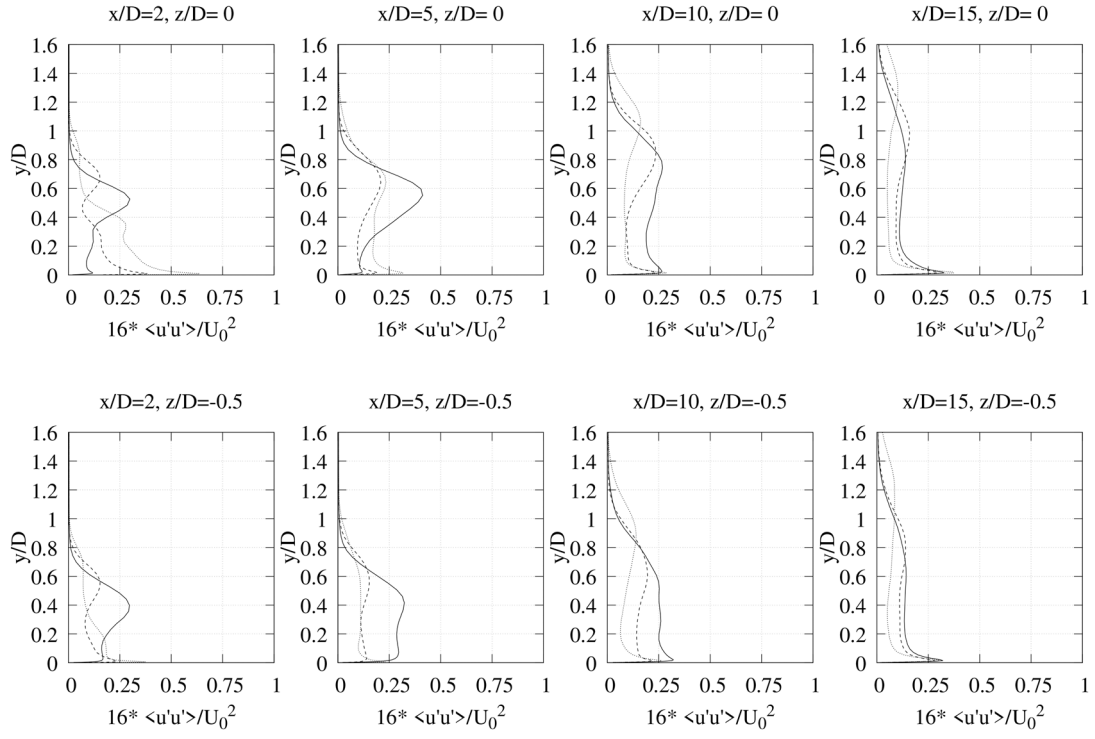

(b) Cylindrical film

Fig. 22. The distribution of Reynolds stresses $< u'u' >$ normalized by the freestream velocity squared at different locations downstream of the fan-shaped and cylindrical films. (Solid line: M=0.5; dash line: M=1.0; dot line: M=1.5).

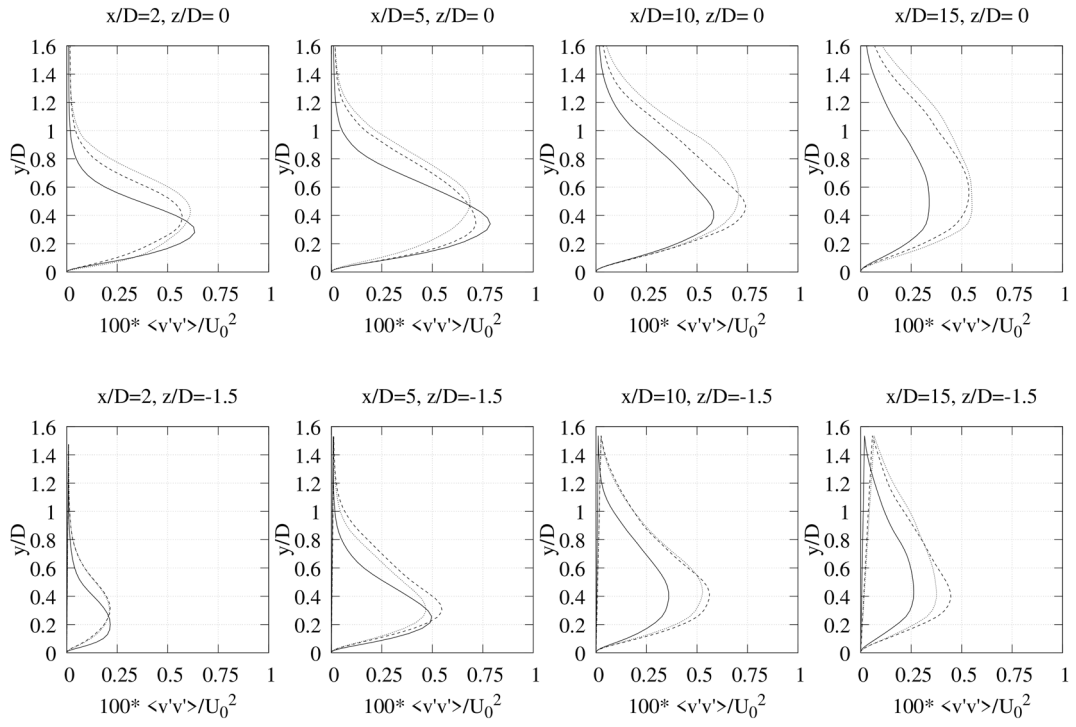

(a) Fan-shaped film

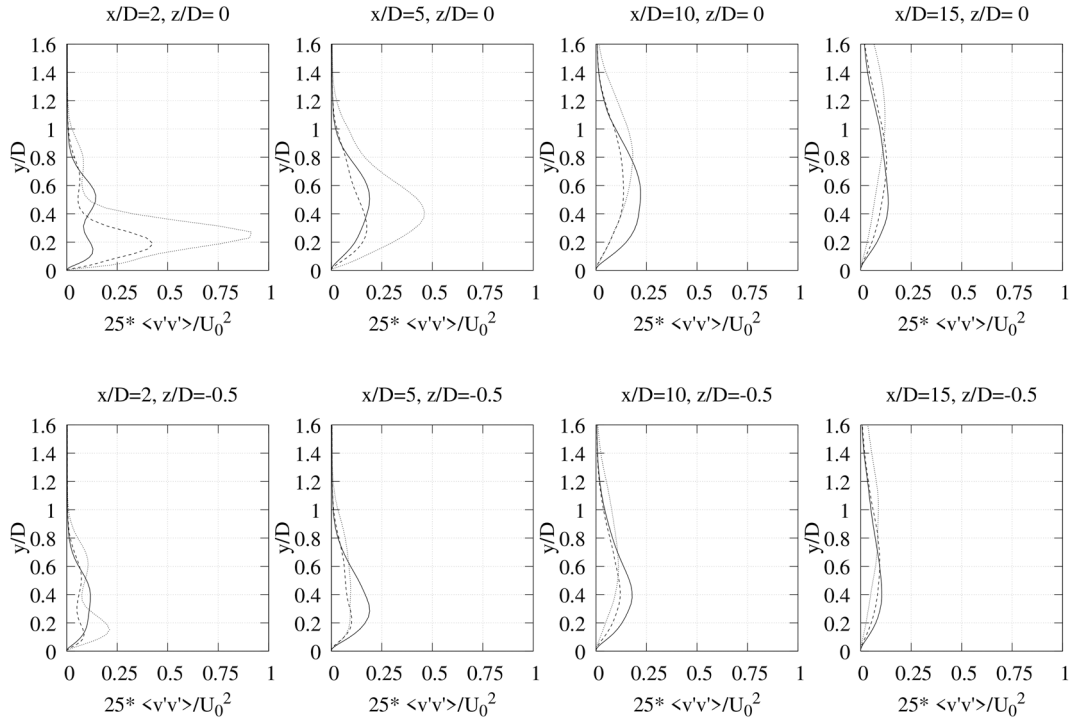

(b) Cylindrical film

Fig. 23. The distribution of Reynolds stresses $< v'v' >$ normalized by the freestream velocity squared at different locations downstream of the fan-shaped and cylindrical films. (Solid line: M=0.5; dash line: M=1.0; dot line: M=1.5)

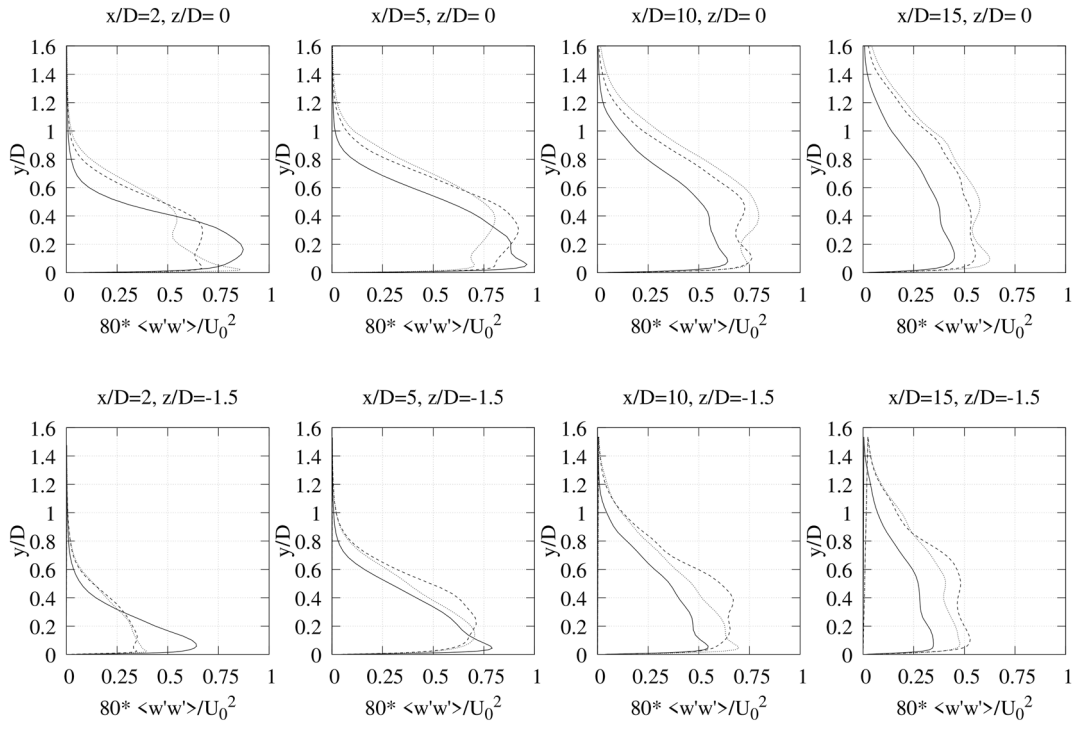

(a) Fan-shaped film

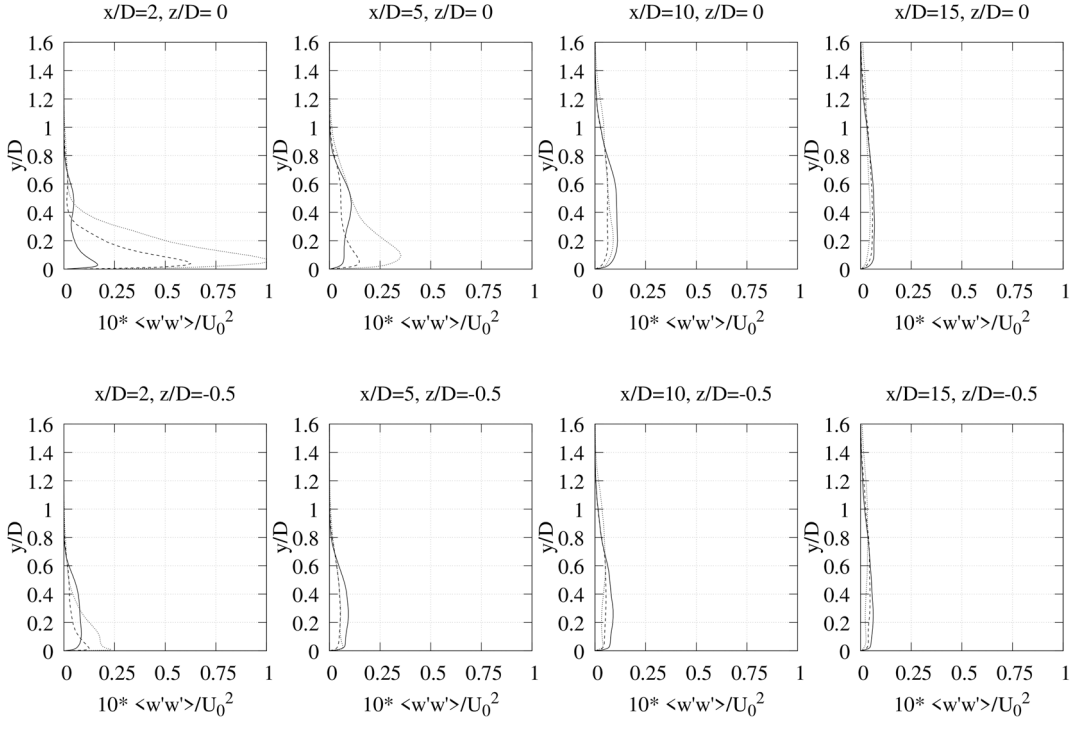

(b) Cylindrical film

Fig. 24. The distribution of Reynolds stresses $< w'w' >$ normalized by the freestream velocity squared at different locations downstream of the fan-shaped and cylindrical films. (Solid line: M=0.5; dash line: M=1.0; dot line: M=1.5).

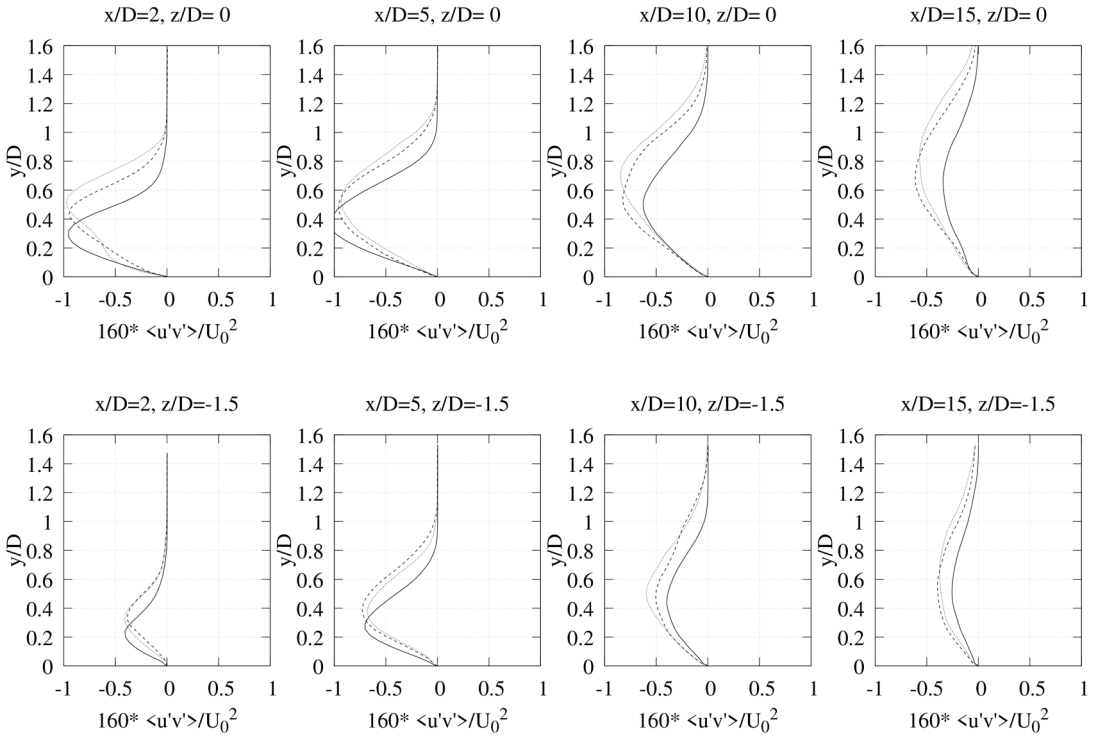

(a) Fan-shaped film

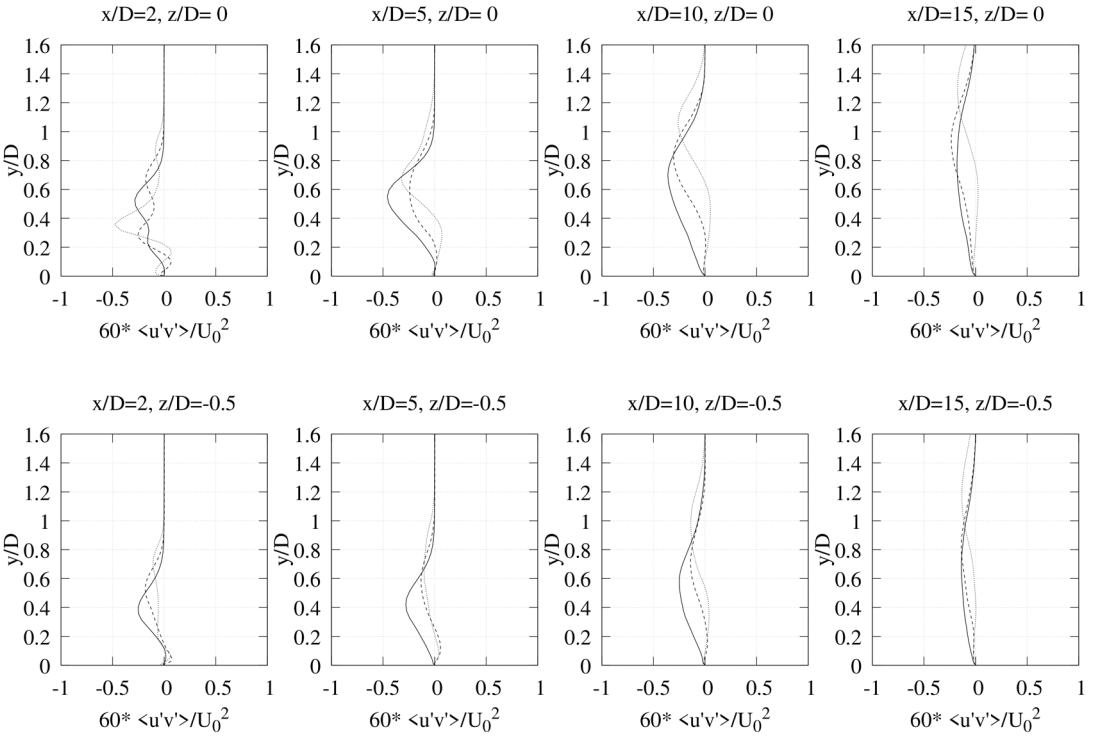

(b) Cylindrical film

Fig. 25. The distribution of Reynolds shear stresses $< u'v' >$ normalized by the freestream velocity squared at different locations downstream of the fan-shaped and cylindrical films. (Solid line: M=0.5; dash line: M=1.0; dot line: M=1.5).

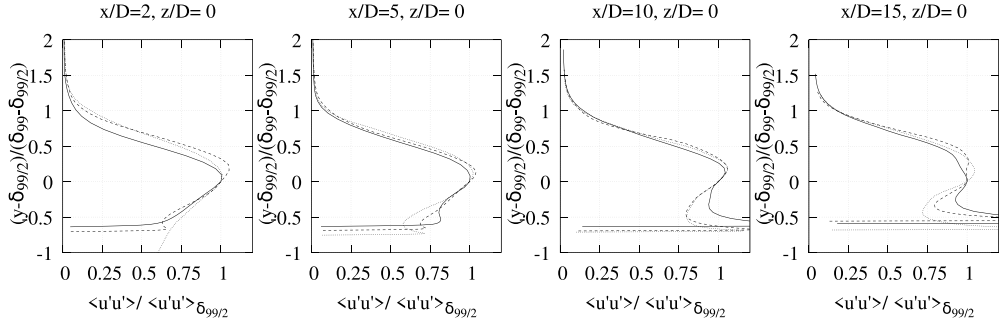

(a) <u'u'>

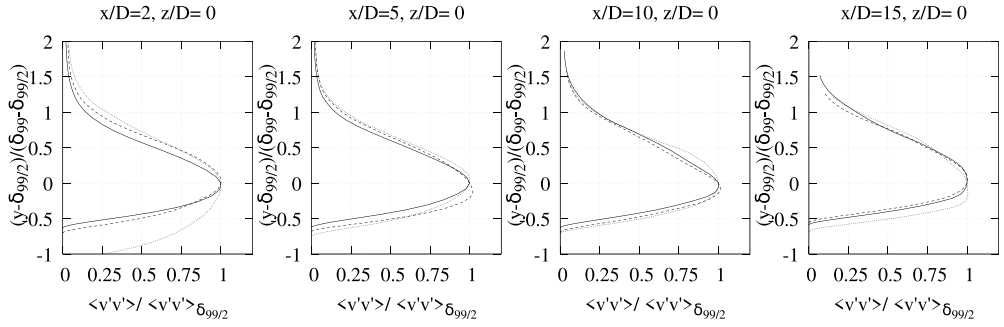

(b) <v'v'>

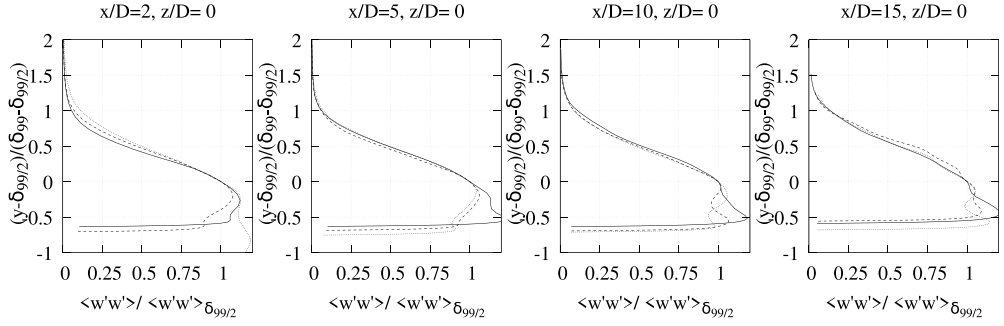

(c) <w'w'>

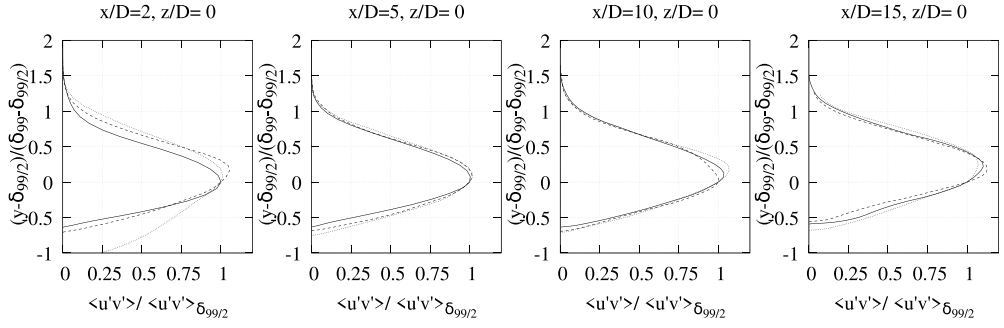

(d) <u'v'>

Fig. 26. Profiles of the Reynolds stress (a)$< u'u' >$, (a)$< v'v' >$, (a)$< w'w' >$ and (a)$< u'v' >$ normalized by corresponding Reynolds stress component at the core of the jet $\delta_{99}/2$ in the fan-shaped film(Solid line: M=0.5; dash line: M=1.0; dot line: M=1.5).

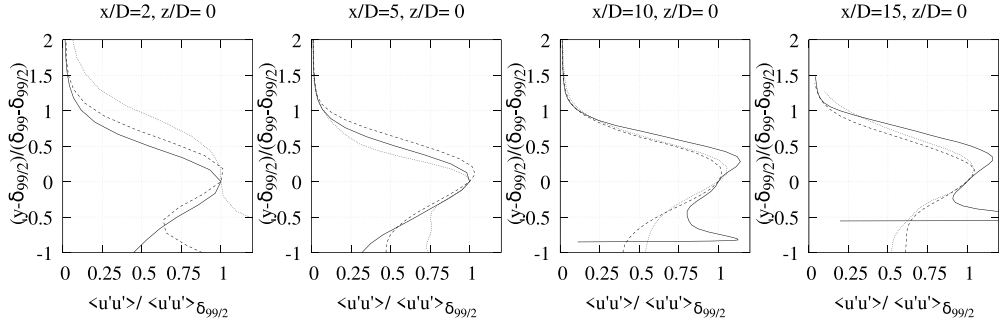

(a) <u'u'>

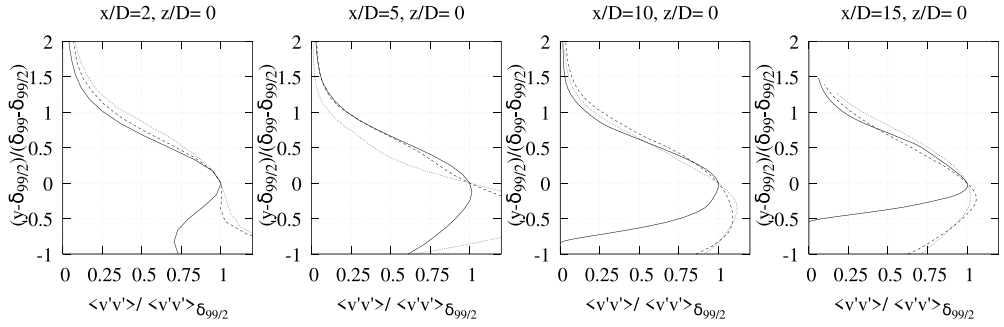

(b) <v'v'>

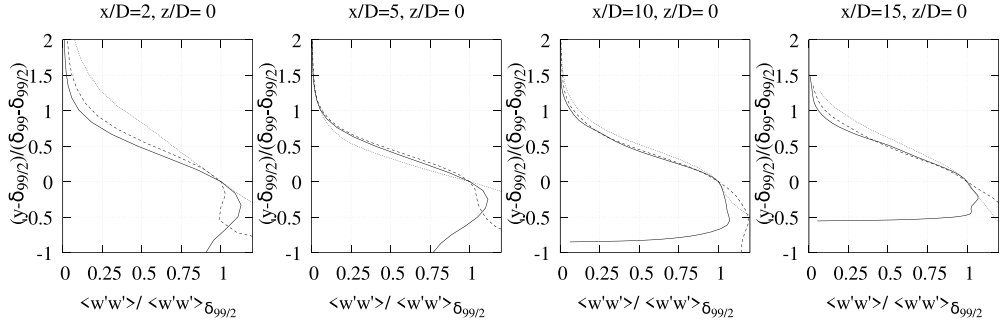

(c) <w'w'>

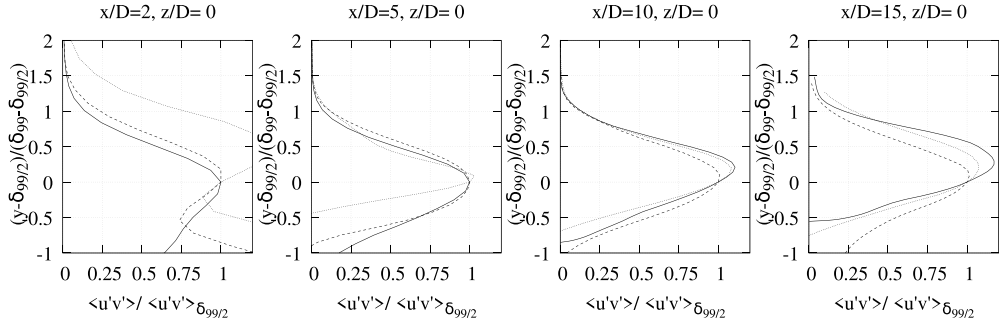

(d) <u'v'>

Fig. 27. Profiles of the Reynolds stress (a)$< u'u' >$, (a)$< v'v' >$, (a)$< w'w' >$ and (a)$< u'v' >$ normalized by corresponding Reynolds stress component at the core of the jet $\delta_{99}/2$ in the cylindrical film(Solid line: M=0.5; dash line: M=1.0; dot line: M=1.5).

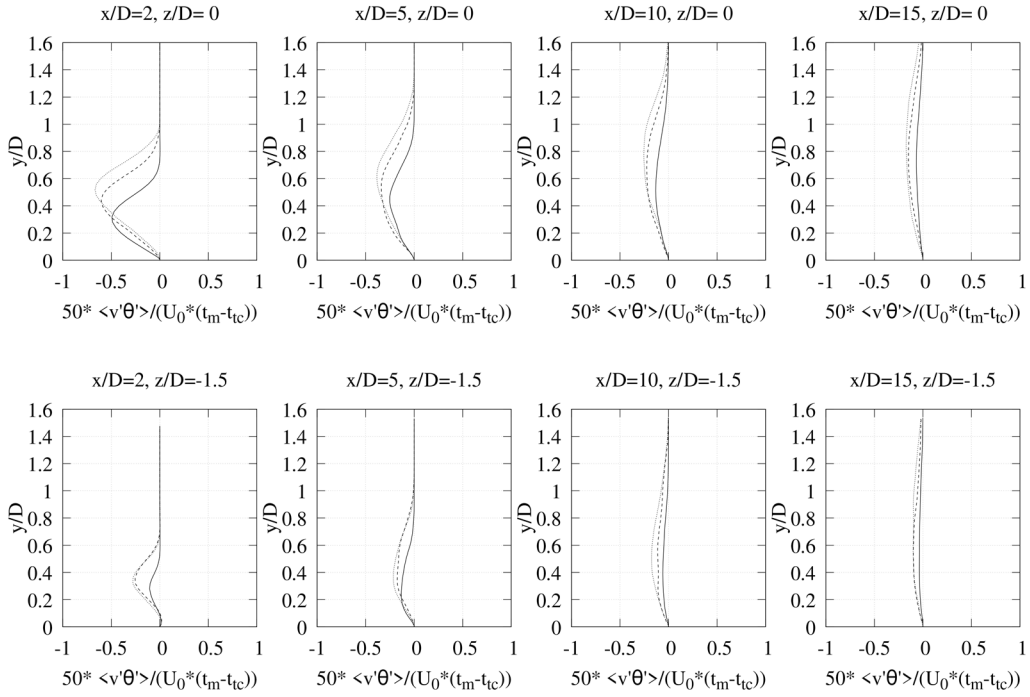

(a) Fan-shaped hole

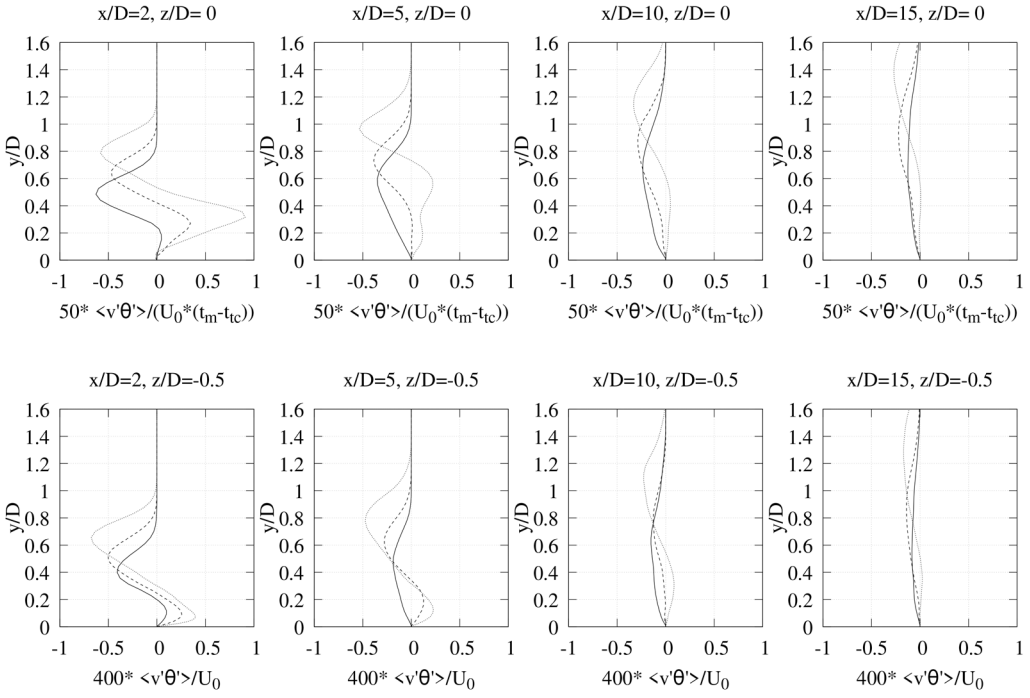

(b) Cylindrical hole

Fig. 28. The distribution of turbulent heat flux in the wall-normal direction in two types of cooling films. Solid line: M=0.5; dash line: M=1.0; dot line: M=1.5.

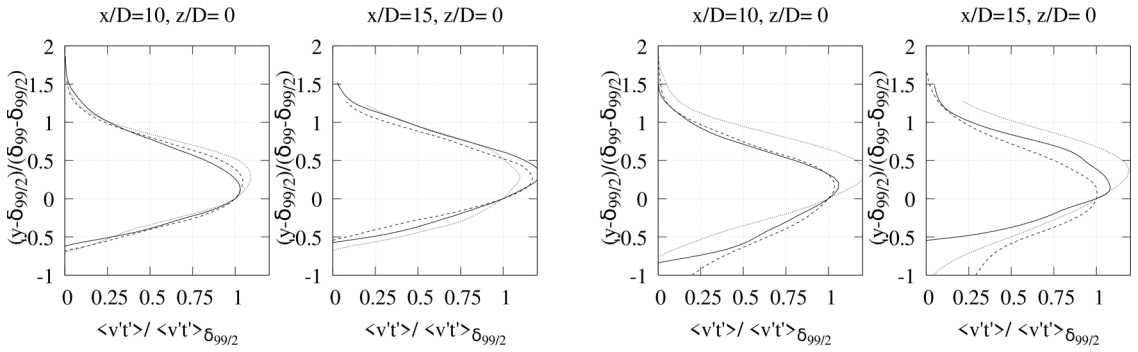

Fig. 29. Profiles of turbulent heat flux in the wall-normal direction $< v't' >$ in two types of cooling films. normalized by the corresponding turbulent heat flux at the core of the jet $\delta_{99}/2$ (Solid line: M=0.5; dash line: M=1.0; dot line: M=1.5).

in turbulent heat flux in the far-field region as long as the suitable scaling method is adopted.

5. Conclusion

A large number of published results focus on quantities of direct interest to the cooling system designer such as the film cooling effectiveness but overlook detailed distributions of the velocity and the Reynolds stress in the flow above the cooled surface. Velocity fields and Reynolds stress distributions are nonetheless the factors that ultimately determine the film cooling effectiveness by deciding the concentration of coolant near the surface.

This study uses LES to investigate the mean flow, Reynolds stress, and turbulent heat flux distributions of a well-documented set of experiments on film cooling. LES simulations are performed on fan-shaped and cylindrical films at blowing ratios of 0.5, 1.0, and 1.5 when the free-stream Mach number is 0.6. The simulations are validated against 1) published discharge characteristics; 2) published velocity and turbulence intensity profiles measured on the same flow configurations.

The results show that:

- LES simulations of modest cost can reproduce with high accuracy the measured discharge characteristics of cylindrical and fan-shaped cooling films.
- The mean velocity and temperature fields produced by a fan-shaped film approach a self-similar flow profile very rapidly downstream of the injection point. The mean velocity and temperature fields produced by a cylindrical film only approach self-similar profiles at low blowing ratios or at high blowing ratios, but not at intermediate blowing ratios (~ 1).
- The similarity variables are the local velocity defect and temperature deficit and the jet layer thickness. These similarity relations only apply to the outer part of the jet.
- The jets acquire a layered structure with a developing boundary layer confined between the jet and the wall, and a free shear layer separating the jet from the mainstream.
- Analysis of the Reynolds stress and turbulent heat flux profiles shows that turbulent quantities do not reach self-similar behavior when scaled with the local velocity defect and jet layer thickness.
- The Reynolds stress and turbulent heat flux profiles show that the section of the jet resembling a free shear layer has essentially uniform and fairly isotropic Reynolds stress and has a distinct behavior from the boundary layer growing between the wall and the jet itself.
- The Reynolds stress and turbulent heat flux profiles can show the self-similarity pattern as long as suitable scaling methods are adopted.

Furthermore, the flow downstream of roughly 5*D* is not particularly challenging to model (from the observation of self-similarity) and the real difficulties of simulating accurately happen within the first 5*D*. There have been RANS-based results (Fig. 14 in [10]) showing that in most cases RANS predictions contain the correct asymptotic decay of quantities such as effectiveness, but the wrong level. The regions where inaccuracies of previous studies are most likely in the near-field downstream of the film exit. It is in this region that deviations from self-similarity and strong three-dimensional flows are encountered, and it is in this region that RANS models are most likely to struggle. The evolution of the coolant jet far downstream of this region is not particularly problematic because the mean flow becomes self-similar and nearly two-dimensional. The indications obtained from the results in this paper are that the velocity and temperature profiles do not attain a self-similar behavior within 5 film diameters from the injection point. As a consequence quality of RANS predictions is almost entirely determined by the quality of the prediction in the near-field region of the film, which is also the least favorable to the properties of linear turbulence models. Therefore, in the presence of self-similar flow, it is possible to match a RANS prediction of a slowly varying flow quantity by modifying a single parameter in a model (see Wilcox [33] on asymptotic analysis in boundary layers). Therefore, this indicates that, with the self-similarity discovered in this study, as long as the quality of RANS predictions within the distance of five diameters can be improved by modifying a single parameter in a model, the expensive cost of LES could be avoided when maintaining the quality of prediction. More analysis regarding the self-similarity based on this study can be found in Hao and Mare [34] and Hao and Mare [35].

Declaration of Competing Interest

The authors have no conflicts to disclose.

CRediT authorship contribution statement

Muting Hao: Conceptualization, Data curation, Investigation, Methodology, Software, Validation, Visualization, Writing – original draft, Writing – review & editing. **Luca di Mare:** Conceptualization, Funding acquisition, Project administration, Supervision, Methodology, Writing – review & editing.

Data availability

Data will be made available on request.

Acknowledgments

This work was finished under the sponsoring by Rolls-Royce plc. Rolls-Royce plc is gratefully acknowledged for supporting this work and for granting permission for its publication. The authors sincerely thank Romero Eduardo, Frederic Goenaga, and Cristian Orozco Pineiro in Rolls-Royce plc for helpful discussion. The authors also acknowledge the use of the University of Oxford Advanced Research Computing (ARC) facility in carrying out this work. www.dx.doi.org/10.5281/zenodo.22558 Part of this work was also performed using resources provided by the Cambridge Service for Data Driven Discovery (CSD4) operated by the University of Cambridge Research Computing Service www.csd3.cam.ac.uk, provided by Dell EMC and Intel using Tier-2 funding from the Engineering and Physical Sciences Research Council (capital grant EP/T022159/1), and DiRAC funding from the Science and Technology Facilities Council www.dirac.ac.uk.

References

[1] A. Hoda, S. Acharya, Predictions of a film coolant jet in crossflow with different turbulence models, J Turbomach 122 (3) (1999) 558–569, doi:10.1115/1.1302322.
[2] J. Ziefle, L. Kleiser, Assessment of a film-cooling flow structure by large-eddy simulation, J. Turbul. 9 (2008) N29, doi:10.1080/14685240802232855.
[3] A.K. Sinha, D.G. Bogard, M.E. Crawford, Film-cooling effectiveness downstream of a single row of holes with variable density ratio, J Turbomach 113 (3) (1991) 442–449, doi:10.1115/1.2927894.
[4] X. Guo, W. Schröder, M. Meinke, Large-eddy simulations of film cooling flows, Computers & Fluids 35 (6) (2006) 587–606, doi:10.1016/j.compfluid.2005.02.007.
[5] P. Renze, W. Schröder, M. Meinke, Large-eddy simulation of film cooling flows with variable density jets, Flow, Turbulence and Combustion 80 (1) (2007) 119–132, doi:10.1007/s10494-007-9080-8.
[6] L. Gräf, L. Kleiser, Large-eddy simulation of double-row compound-angle film cooling: setup and validation, Computers & Fluids 43 (1) (2011) 58–67, doi:10.1016/j.compfluid.2010.09.032.
[7] X. Kong, Y. Zhang, G. Li, X. Lu, J. Zhu, J. Xu, Heat transfer and flow structure characteristics of film-cooled leading edge model with sweeping and normal jets, Int. Commun. Heat Mass Transfer 138 (2022) 106338, doi:10.1016/j.icheatmasstransfer.2022.106338.
[8] X. Chen, Y. Long, Y. Wang, S. Weng, Y. Luan, Large eddy simulation of film cooling from cylindrical holes partially blocked by CaO-MgO-al2o3-SiO2, Int. Commun. Heat Mass Transfer 129 (2021) 105754, doi:10.1016/j.icheatmasstransfer.2021.105754.
[9] Y. Wang, W. Wang, G. Tao, X. Zhang, S. Luo, J. Cui, Two-dimensional film-cooling effectiveness prediction based on deconvolution neural network, Int. Commun. Heat Mass Transfer 129 (2021) 105621, doi:10.1016/j.icheatmasstransfer.2021.105621.
[10] Y. Jiang, A. Murray, L.d. Mare, P. Ireland, Mesh sensitivity of RANS simulations on film cooling flow, Int J Heat Mass Transf 182 (2022) 121825, doi:10.1016/j.ijheatmasstransfer.2021.121825.
[11] S. Wittig, A. Schulz, M. Gritsch, K.A. Thole, Transonic film-cooling investigations: Effects of hole shapes and orientations, Volume 4: Heat Transfer Electric Power Industrial and Cogeneration, American Society of Mechanical Engineers, 1996, doi:10.1115/96-gt-222.
[12] K. Thole, M. Gritsch, A. Schulz, S. Wittig, Flowfield measurements for film-cooling holes with expanded exits, J Turbomach 120 (2) (1998) 327–336, doi:10.1115/1.2841410.
[13] M. Gritsch, A. Schulz, S. Wittig, Adiabatic wall effectiveness measurements of film-cooling holes with expanded exits, J Turbomach 120 (3) (1998) 549–556, doi:10.1115/1.2841752.
[14] A. Zamiri, J.T. Chung, Large eddy simulation of internal coolant crossflow orientation effects on film-cooling effectiveness of fan-shaped holes, Int J Heat Mass Transf 190 (2022) 122778, doi:10.1016/j.ijheatmasstransfer.2022.122778.
[15] T.A. Oliver, D.G. Bogard, R.D. Moser, Large eddy simulation of compressible, shaped-hole film cooling, Int J Heat Mass Transf 140 (2019) 498–517, doi:10.1016/j.ijheatmasstransfer.2019.04.119.
[16] W.-S. Fu, W.-S. Chao, M. Tsubokura, C.-G. Li, W.-H. Wang, Direct numerical simulation of film cooling with a fan-shaped hole under low reynolds number conditions, Int J Heat Mass Transf 123 (2018) 544–560, doi:10.1016/j.ijheatmasstransfer.2018.03.011.
[17] A. Zamiri, G. Barigozzi, J.T. Chung, Large eddy simulation of film cooling flow from shaped holes with different geometrical parameters, Int J Heat Mass Transf 196 (2022) 123261, doi:10.1016/j.ijheatmasstransfer.2022.123261.
[18] S. Agarwal, L. Gicquel, F. Duchaine, N. Odier, J. Dombart, Analysis of the unsteady flow field inside a fan-shaped cooling hole predicted by large eddy simulation, J Turbomach 143 (3) (2021), doi:10.1115/1.4050121.
[19] A. Kohli, D.G. Bogard, Turbulent transport in film cooling flows, J Heat Transfer 127 (5) (2005) 513–520, doi:10.1115/1.1865221.
[20] M. Gritsch, A. Schulz, S. Wittig, Discharge coefficient measurements of film-cooling holes with expanded exits, J Turbomach 120 (3) (1998) 557–563, doi:10.1115/1.2841753.
[21] K.A. Thole, M. Gritsch, A. Schulz, S. Wittig, Effect of a crossflow at the entrance to a film-cooling hole, J Fluids Eng 119 (3) (1997) 533–540, doi:10.1115/1.2819277.
[22] M. Gritsch, C. Saumweber, A. Schulz, S. Wittig, E. Sharp, Effect of internal coolant crossflow orientation on the discharge coefficient of shaped film-cooling holes, J Turbomach 122 (1) (1999) 146–152, doi:10.1115/1.555436.
[23] M. Gritsch, A. Schulz, S. Wittig, Effect of crossflows on the discharge coefficient of film cooling holes with varying angles of inclination and orientation, J Turbomach 123 (4) (2001) 781–787, doi:10.1115/1.1397306.
[24] C. Saumweber, A. Schulz, S. Wittig, M. Gritsch, Effects of entrance crossflow directions to film cooling holes, Ann. N. Y. Acad. Sci. 934 (1) (2006) 401–408, doi:10.1111/j.1749-6632.2001.tb05876.x.
[25] C. Saumweber, A. Schulz, Effect of geometry variations on the cooling performance of fan-shaped cooling holes, J Turbomach 134 (6) (2012), doi:10.1115/1.4006290.
[26] M. Hao, F. Wang, J. Hope-Collins, M.E. Rife, L.d. Mare, Template-based hexahedral mesh generation for turbine cooling geometries, in: Volume 2C: Turbomachinery, American Society of Mechanical Engineers, doi:10.1115/gt2020-14660.
[27] M. Čada, M. Torrilhon, Compact third-order limiter functions for finite volume methods, J Comput Phys 228 (11) (2009) 4118–4145, doi:10.1016/j.jcp.2009.02.020.
[28] M. Hao, J. Hope-collins, L.d. Mare, Generation of turbulent inflow data from realistic approximations of the covariance tensor, Physics of Fluids (2022), doi:10.1063/5.0106664.
[29] K.W. Thompson, Time dependent boundary conditions for hyperbolic systems, J Comput Phys 68 (1) (1987) 1–24.
[30] A.A. Townsend, The properties of equilibrium boundary layers, J Fluid Mech 1 (06) (1956) 561, doi:10.1017/s0022112056000378.
[31] M. Hoffmeister, Townsend, A. A., the structure of turbulent shear flow, second edition, cambridge. cambridge university press. 1976. 429 s., £ 15.50 a. cambridge monographs on mechanics and appl. mathematics, ZAMM - Zeitschrift für Angewandte Mathematik und Mechanik 56 (9) (1976) 448, doi:10.1002/zamm.19760560921.
[32] T.A. Girshovich, The turbulent jet in a cross flow, Fluid Dyn. 1 (1) (1967) 108–109, doi:10.1007/bf01016285.
[33] J.W. Wilcox, The p/b-ROE valuation model, Financial Analysts Journal 40 (1) (1984) 58–66, doi:10.2469/faj.v40.n1.58.
[34] M. Hao, L.d. Mare, Budgets of Reynolds stresses in film cooling with fan-shaped and cylindrical holes, Physics of Fluids (2023), doi:10.1063/5.0140670.
[35] M. Hao, L.d. Mare, Scaling and similarity laws in three-dimensional wall jets, Physics of Fluids (2023), doi:10.1063/5.0140671.